ACS Catalysis

Research Article

pubs.acs.org/acscatalysis

SP20 Phosphorylation Reaction Catalyzed by Protein Kinase A: QM/MM Calculations Based on Recently Determined Crystallographic Structures

Ayax Pérez-Gallegos, Mireia Garcia-Viloca, Àngels González-Lafont,* and José M. Lluch

Institut de Biotecnologia i de Biomedicina and Departament de Química, Universitat Autònoma de Barcelona, 08193 Bellaterra, Barcelona, Spain

Supporting Information

ABSTRACT: The cAMP-dependent protein kinase (PKA) has been the most studied human protein kinase ever. Very recently, new X-ray crystallographic structures in which the SP20 substrate has been trapped in the ternary complex with PKA before and after the phosphoryl transfer have provided a few tentative snapshots of the evolution of the enzyme system along the catalytic reaction. In the present paper, we have studied the dissociative and the associative mechanisms for the phosphorylation reaction of the SP20 substrate catalyzed by PKA by means of MP2/aug-cc-pVTZ/CHARMM//B3LYP/6-31+G(d)/CHARMM electronic structure calculations using a complete solvated model of the PKAc-ATPMg$_2$−SP20 system. Our results demonstrate that the dissociative mechanism (involving two consecutive steps: phosphoryl transfer and back protonation of the phosphorylated substrate) is clearly more favorable than the associative one. A comparison of Kemptide with SP20 shows that the catalytic mechanism is not substrate-dependent. However, the product complexes are better stabilized in the active site in the case of SP20, which may explain why phosphokemptide dissociates much faster. We show for the first time the viability of the SP20 phosphorylation process in a conformation of the PKAc-ATPMg$_2$−SP20 ternary complex in which the Gly-rich loop is displaced with respect to the fully closed conformation of the PKAc-ATPMg$_2$−IP20. Lastly, we provide a complete sequence of the geometrical evolution of the structure of the ternary complex along the catalytic reaction. This permits the identification of the snapshots corresponding to the above-mentioned new X-ray crystallographic structures, so validating the atomic view of the reaction suggested by them.

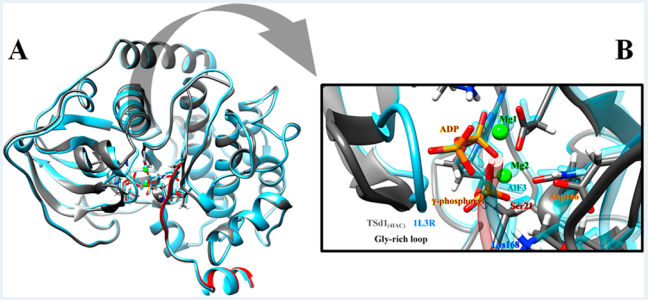

KEYWORDS: *enzyme catalysis, protein kinase A, phosphorylation reactions, general acid/base catalysis, associative mechanism, dissociative mechanism, QM/MM calculations*

1. INTRODUCTION

Protein phosphorylation is a central process in regulation and cell signaling. Protein kinases are the enzymes that catalyze the transfer of a phosphoryl group from adenosine triphosphate (ATP) to the side chains of a particular serine, threonine, or tyrosine residue. The malfunctioning of many protein kinases has been associated with a multitude of diseases, such as cancer, metabolic disorders, and inflammation; hence, protein kinases have emerged as important therapeutic targets.[1] Among human kinases, cAMP-dependent protein kinase (PKA) was the first to be characterized,[2,3] and it has also been the most analyzed ever since, becoming a framework for the whole kinase family.[4,5]

One of the most intriguing aspects of protein kinases has to do with the mechanisms that regulate their activity. In this respect, the study of the enzyme conformational changes that take place along the catalytic cycle has attracted a great deal of attention over the years.[4,6,7] It has long been recognized that protein kinases experience large conformational changes that involve the narrowing (closing) of the active site cleft formed by two adjacent lobes, a small lobe (N-terminal) and a large one (C-terminal). A large number of crystallographic structures have been reported that range from open to closed conformations going through the so-called "intermediate" conformations.[4] Three specific distances have been used to distinguish the structure of closed from open conformations: the Glu170-Tyr330 distance measures the distance of the C-terminal tail to the active site, the His87 to phospho-Thr197 distance measures the position of the C-helix relative to the large lobe, and the Ser53-Gly186 distance that measures the opening and closing of the glycine-rich loop.[2] This flexible Gly-rich loop, which functions as a lid on top of the ATP phosphates, is the most mobile motif in the PKA catalytic subunit (PKAc) and can experience a displacement as big as 6.5 Å in going from the open to the closed conformation.[8] Mutagenesis experiments have also been used to analyze the role of this loop in the catalytic activity of PKA.[9] In this respect,

Received: May 20, 2015
Revised: July 8, 2015
Published: July 9, 2015

DOI: 10.1021/acscatal.5b01064
ACS Catal. 2015, 5, 4897−4912

it has been shown that the interaction between the backbone amide of Ser53, at the tip of the glycine-rich loop, with the γ-phosphate of ATP in the closed conformation of the wild-type enzyme is relevant for the nucleotide binding process, whereas the Ser53 side chain is not required at all for the phosphorylation of a peptide substrate.

The conformational change of PKAc initiates with the *apo* form (without ATP or substrate bound) in an open conformation. It partially closes when ATP binds to give a binary PKAc-ATP complex, with an active site that is primed for substrate binding. The PKAc-ATP-substrate in the closed conformation is the ternary enzymatic state poised for phosphorylation of the target substrate. In accordance with experimental observations, molecular dynamics (MD) trajectories[8] initiated with the closed PKAc-ATP-PKI (inhibitor) conformation, have simulated the opening of the active site cleft of PKAc when both ligands are removed, regardless of the kinase phosphorylated state at Thr197 and Ser338. Those simulations also show that the most stable state is the closed ternary complex, whereas all the other systems with one or two ligands removed visit different conformations along the MD trajectory.

Moreover, NMR measurements together with thermodynamic data and Principal Components Analysis carried out on MD simulations of PKAc in water using the *apo*, binary (nucleotide bound), and ternary complexes (containing the native substrate PLN_{1-20} or the inhibitor PKI_{5-24}) have shown that PKAc has an intrinsic dynamic nature behaving as a regulated molecular switch.[6,10,11] Those studies have been used to characterize the conformational dynamic states of PKAc along its catalytic cycle, describing the free-energy landscape for PKAc in which the *apo* form would correspond to the so-called dynamically uncommitted state, where motions are present but not on a time scale relevant for turnover. In contrast, the nucleotide-bound or the Michaelis complex with the substrate, would correspond to dynamically committed states, where motions are synchronous with the rate-limiting step of enzyme turnover. Although these motions are slower than the chemical step (phosphoryl transfer), they help to position the substrate for catalysis giving access to those enzyme conformations that facilitate turnover. Finally, the inhibited complexes have been characterized as dynamically quenched states where the enzyme dynamics are hindered. This result may explain, according to the authors, why most crystal structures of protein kinases have been more accessible in their inhibited forms while substrate bound forms have been elusive to such analyses.

Nevertheless, very recently also, a new X-ray crystallographic structure has been deposited in the Protein Data Bank (PDB) in which the 20-residue SP20 substrate has been successfully cocrystallized in PKAc with AMP-PCP in a pseudo-Michaelis complex conformation (PDB code 4IAC).[12] The other three X-ray crystallographic structures correspond to crystals in which both products (ADP, and the phosphorylated SP20 peptide) have been trapped (PDB codes: 4IAF, 4HPU, 4HPT).[12,13] The molecular information obtained from those structures has been used, together with the transition state (TS) mimic structure (PDB code 1L3R),[14] to reveal new insights on the reaction mechanism of the phosphoryl transfer process catalyzed by PKAc. The role of metals in the chemical step as well as in the rate-limiting step of ADP release has been revised in PKAc and other kinases.[12,13,15−17] As for the characteristics of the phosphoryl transfer mechanism, Gerlits et al.[12] interpret their crystallographic structures, 4IAC and 4IAF, as snapshots of a mechanism in which the OH group of $Ser21_{SP20}$ would experience a rotation movement (denominated by the authors, the "driving force of the reaction") from its location in the Michaelis complex structure 4IAC, where the substrate's OH group is hydrogen-bonded to the γ-phosphate but away from Asp166, to its orientation at the 1L3R TS mimic where the hydroxyl side chain of $Ser21_{SP20}$ is now hydrogen-bonded to Asp166. After the phosphoryl transfer, in the configuration represented by the 4IAF structure, the transferred phosphate group at pSP20 would rotate toward the solvent moving away again from Asp166. Gerlits et al.[12] validate the orientation of the hydroxyl side chain of $Ser21_{SP20}$ in the 4IAC X-ray crystallographic structure by indicating that it had been found before in MD simulations of the PKAc-ATPMg_2−SP20 Michaelis complex initiated from the 1CDK structure, by some of the authors of the present paper.[18] Moreover, a physiological relevance is given to that particular orientation of the $Ser21_{SP20}$ side chain because it has also been observed in the crystallographic structure of the tetrameric PKA RIIβ holoenzyme−products complex.[19] However, the mechanistic pathway proposed by Gerlits et al.[12] from their crystallographic data for the phosphorylation of SP20 in PKAc does not agree with previous experimental and theoretical studies with SP20 or other ligands,[20−32] which had put forward the active role of Asp166 as a general base or acid/base catalyst. It has also been asserted, however, that the phosphoryl transfer mechanism might be substrate-dependent.

In our previous studies[30,32,33] a detailed theoretical study of the associative and dissociative phosphorylation mechanisms of the synthetic substrate Kemptide by PKAc has been carried out. We named there the dissociative and the associative mechanisms adopting the definition given by Warshel and coworkers for a phosphate monoester hydrolysis in aqueous solution.[34,35] That is, the dissociative mechanism implies an almost complete break of the bond between the ADP and the metaphosphate leaving group before the new bond with the nucleophile serine residue begins to be formed. Conversely, in the associative mechanism, the bond formation with the substrate serine residue starts when the ADP and the γ-phosphate leaving group are still quite closely connected. According to the IUPAC nomenclature, the dissociative and associative mechanisms are both concerted mechanisms (A_ND_N). The transition state nature, which can be described as loose or tight, is the difference between both mechanisms. Our results demonstrated that the dissociative mechanism with Kemptide, in which the Asp166 residue behaves as a general acid/base catalyst, is more favorable than the associative one. The phosphoryl transfer potential energy profiles were calculated from prereactive minima obtained from snapshots of an MD simulation of the solvated PKAc-ATPMg_2−Kemptide Michaelis complex. The initial model was built from the X-ray crystallographic coordinates of the closed ternary complex PKAc-ATPMg_2−PKI (PDB code 1CDK),[9] where PKI is the heat-stable protein inhibitor of PKA.

At this point, the new X-ray crystallographic structures of Gerlits et al.[12] in which the SP20 substrate is trapped in the ternary complex, before and after the phosphoryl transfer, have provided very valuable structural information which is not biased by any inhibitor molecule. However, the experimental mechanistic conclusions extracted from that crystallographic data urge for new theoretical calculations that could analyze those proposals by means of an accurate phosphoryl transfer simulation at the molecular level. In this paper, we present high

DOI: 10.1021/acscatal.5b01064
ACS Catal. 2015, 5, 4897−4912

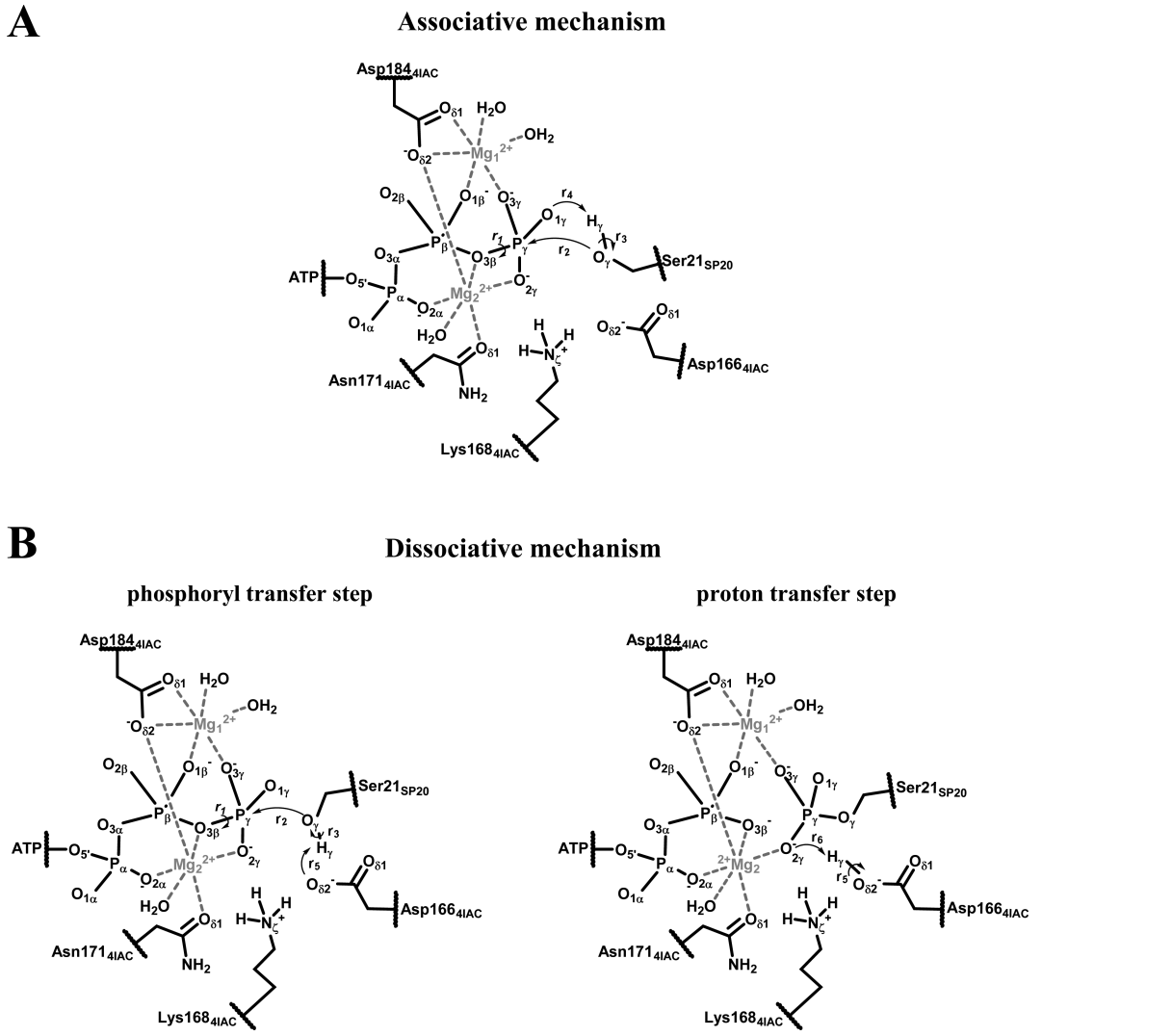

Figure 1. Scheme of the proposed mechanisms for PKA. (A) Associative mechanism. (B) Dissociative mechanism: phosphoryl and proton transfer steps. All QM atoms within PKA's active site are represented, except the side chains' hydrogen atoms. The wavy lines stand for the frontier between QM and MM regions.

level QM/MM calculations of the SP20 phophorylation reaction catalyzed by PKAc. A complete solvated model of the ternary complex PKAc-ATPMg_2−SP20 has been built from the 4IAC X-ray crystallographic structure. Both the associative and the dissociative mechanisms have been analyzed, and a detailed comparison with the experimental structural data is given in an effort to accommodate the enzyme−substrate, the enzyme−product, and the earlier transition-state mimic crystallographic structures, as Gerlits et al.[12] themselves suggest, on the proper molecular reaction pathway.

2. MODELS AND METHODS

Coordinates from the X-ray crystallographic structure with PDB code 4IAC[12] were used to start modeling the Michaelis complex of PKA with its ligands at the beginning of the phosphoryl transfer chemical step. Specifically, this 2.15 Å resolution crystallographic structure contains the enzyme catalytic subunit, the unhydrolyzable ATP analogue adenosine-5′-[β,γ-Methylene]triphosphate (AMP-PCP), the 20-residue SP20 substrate, the two Mg^{2+} ions, and 339 crystallographic water molecules. That is, the reactive complex in the 4IAC structure represents a pseudo-Michaelis complex because it lacks the actual ATP cofactor.[12] In our model the ATP nucleotide was modeled by substituting the β,γ-bridging carbon atom in AMP-PCP by an oxygen atom. The triphosphorylated state (pSer139, pThr197, and pSer338) of PKA in the 4IAC structure was kept to build up our model of the Michaelis complex given that it represents an active configuration of the enzyme's catalytic subunit.

Because the reaction happens at physiologic pH, all titratable residues were set to their normal ionization state at pH 7. As a result, all Lys and Arg side chains are in the ammonium or guanidinium forms, respectively, and all Asp and Glu side chains are in the carboxylate form. Regarding the protonation state of the histidine residues of the kinase and peptide substrate, the choice was based on the work of Diaz and Field.[25] Thus, for PKA, the residues His68, His142, His158, and His260 were protonated at Nδ, the residues His62, His131, and His294 were protonated at Nε, and the residue His87 was doubly protonated. The histidine present in the P+2 position of the SP20 peptide substrate was protonated at its Nε.

The coordinates of the hydrogen atoms added to the crystallographic heavy atoms were calculated making use of the HBUILD facility[36] implemented in the CHARMM pro-

DOI: 10.1021/acscatal.5b01064
ACS Catal. 2015, 5, 4897−4912

gram.[37,38] The origin of the system was then adjusted to the geometric center of the Oδ2Asp166, Pγ ATP, and Oγ Ser21$_{SP20}$ group of atoms (all within the enzyme's active core). To solvate the structure, a water sphere of 24 Å radius centered at the origin was superimposed on the kinase ternary complex (PKA, ATP, SP20, and Mg^{2+} ions) along with its crystallographic water molecules. Upon insertion, all solvent molecules overlapping or within 2.5 Å of any crystallographic atom were removed, and this was repeated three times with randomly rotated water spheres. Then, to relax energetically unfavorable contacts, a molecular dynamics (MD) simulation (5 ps) of the solvent molecules was carried out. The 3-fold cycle of superposition, deletion, and rotation was then repeated to fill in additional cavities generated from the equilibration calculations. Finally, a second MD solvent equilibration process (5 ps) was performed. Briefly, the MD simulations, for which CHARMM22[39,40] force field was used, were performed at a temperature of 298 K with a leapfrog Verlet algorithm and a time step of 1 fs; also, a nonbonded cutoff of 12 Å was applied, and the bond length and bond angles of all water molecules were constrained by the SHAKE algorithm. The resulting system (8709 atoms) includes the PKA monomer (336 amino acids), one ATP molecule, the SP20 substrate (20 amino acids), two Mg^{2+} ions, and a water sphere with 938 crystallographic and solvent water molecules.

From this solvated enzyme-ATP-substrate model, an initial QM/MM optimization was carried out to avoid any distortions and to eliminate any artifact related with the manipulation of the molecular system. The resulting structure, named i_{model}, was taken as the starting point for all the data presented in this work.

For the QM(DFT)/MM calculations, we have defined the QM/MM partition as follows. All residues and water molecules within 20 Å of the geometric center defined above were included in the optimization process as the active—or allowed to move freely—region, whereas the remainder were kept fixed in their positions along the subsequent optimizations and simulations (4857 and 3852 active and fixed atoms, respectively). The QM region comprised 65 atoms, with a total charge of −1, and included the two magnesium ions, all the residue side chains and water molecules first-coordinating them (i.e., the phosphate groups from the ATP molecule, the side chain of residues Asn171 and Asp184, and three crystallographic waters), the Lys168 side chain, and all the atoms involved in the breaking/forming of chemical bonds, that is, besides the γ-phosphate group of the ATP molecule already included, the Asp166 side chain and, obviously, the Ser21$_{SP20}$ side chain (see Figure 1). All cuts were applied in aliphatic C−C bonds, except that performed in the C5′-O5′ bond of the ATP's ribose, which separates the complete triphosphate tail from the adenosine nucleoside moiety (the latter was treated at the MM level in order to keep the QM region computationally affordable).

All QM/MM calculations were performed with the modular program package ChemShell,[41] using TURBOMOLE[42] to obtain the quantum mechanical (QM) energies and gradients at the DFT level. Specifically, the QM region was treated with the B3LYP[43−48] approximation for the exchange-correlation functional, expanding wave functions by means of Pople's 6-31+G(d) basis set.[49−52] The energies and gradients for the MM region were evaluated by DL_POLY,[53] which was accessed through the ChemShell package using the CHARMM22 force field.[39,40] In previous works, we have shown that the B3LYP functional was a good choice for phosphorus-containing systems,[54] and that the QM(B3LYP/6-31+G(d))/CHARMM level of calculation provided good geometries and energies at reasonable computational time.[32,33] An electronic embedding scheme[53] was adopted in the QM/MM calculations in such a way that the MM point charges were incorporated into the one-electron Hamiltonian during the QM calculation. No cutoffs were introduced for the nonbonding MM and QM/MM interactions. The QM/MM boundary has been treated with the charge-shift model;[55−57] thus, according to the QM region defined above, six hydrogen link atoms were employed to cap the bonds crossing into the MM region. It is widely recognized that the charge-shift scheme reduces the overpolarization of the QM region by the MM point charges within link-atom models.[55−57] Energy minimizations were performed employing the limited-memory Broyden−Fletcher−Goldfarb−Shanno (L-BFGS)[58,59] algorithm (maximum gradient component convergence criterion less than or equal to 0.00045 au), while the transition-state searches were carried out by means of the microiterative optimizer[60,61] combining the L-BFGS and the partitioned rational function optimizer (P-RFO)[62,63] (maximum gradient component convergence criterion less than or equal to 0.00033 au). Both algorithms are implemented in the HDLCopt[61] module of ChemShell. The characteristic single imaginary frequency and the chemically proper transition vector were confirmed for all reported transition states by means of frequency calculations for the QM region. More accurate energy evaluations were obtained by single-point energy calculations at the QM(MP2[64,65]/aug-cc-pVTZ[66,67])/CHARMM level of theory.

First, from the i_{model} starting structure, reaction paths were scanned by constrained QM/MM optimizations along a reaction coordinate in steps of 0.2 Å, according to the equation properly defined for the phosphoryl transfer following an associative mechanism (such equation involves the two antisymmetrical combinations of the bonds to be broken and formed):

$$R4 = r_1 - r_2 + r_3 - r_4 \quad (1)$$

where r_1 is the Oβ ATP−Pγ ATP distance, r_2 is the Oγ Ser21−Pγ ATP distance, r_3 is the Oγ Ser21−Hγ Ser21 distance, and finally, r_4 is the Oiγ ATP−Hγ Ser21 distance (see Figure 1A). Because the γ-oxygen atoms of ATP differ in their chemical environment, the three possibilities (i = 1, 2, 3) were taken into account when modeling the associative reaction path. The reaction coordinates were scanned, going forward and backward (from reactants to products and *vice versa*), until the convergence was reached (i.e., until the potential energy profile of one reaction path and the following were equal). This provided the appropriate starting structures for consequent full QM/MM optimization of all related stationary points (i.e., reactants complex, transition state, and products complex).

On the other hand, from the same i_{model} structure, the dissociative mechanism of the phosphoryl transfer was also simulated by constrained QM/MM optimizations in steps of 0.2 Å according to the reaction coordinate defined as

$$R4 = r_1 - r_2 + r_3 - r_5 \quad (2)$$

where r_5 is the Oδ2Asp166−Hγ Ser21 distance (see Figure 1B, phosphoryl transfer step). The same convergence criterion was applied to the simulated reaction paths and relevant stationary point optimizations from representative geometries were carried out as described above.

DOI: 10.1021/acscatal.5b01064
ACS Catal. 2015, 5, 4897−4912

Subsequently, the optimized product of the dissociative phosphoryl transfer path was then used as the starting structure for scanning the reaction path corresponding to the second step of the dissociative mechanism, that is, the proton (HγSer21) transfer from the just protonated carboxylate group of Asp166 side chain to one of the γ-oxygen atoms of the phosphoryl group already bonded to the substrate $Ser21_{SP20}$. Thus, again in steps of 0.2 Å, constrained QM/MM optimizations were performed along the reaction coordinate defined as

$$R2 = r_5 - r_6 \quad (3)$$

where r_6 is the OiγATP−HγSer21 distance (i = 1, 2, 3) (see Figure 1B, proton transfer step). When it was possible to simulate a converged proton transfer path, it was confirmed that it yielded backward the same optimized phosphoryl transfer product—both geometrically and energetically—as the preceding phosphoryl transfer path. That is, phosphoryl transfer and proton transfer reaction paths are connected through the same molecular complex. Lastly, from the suitable structures in each case, the final products complex of PKA catalyzed phosphoryl transfer reaction was characterized and microiterative QM/MM TS search was performed, as described above. The figures showing molecular structures were generated using VMD version 1.8.7.[68]

3. RESULTS

As mentioned in the Introduction section, the aim of the work presented here is to simulate the phosphoryl transfer step from the pseudo-Michaelis complex analogue PKAc-AMP-PCPMg_2−SP20, determined experimentally by Gerlits et al.,[12] adjusting our initial theoretical model as close as possible to the experimental X-ray model (4IAC[12]) in order to be able to compare our results with it and with the related PKA X-ray structures: the transition state mimic of the catalytic subunit (PDB entry 1L3R[14]), and the product of the phosphoryl transfer reaction (PDB entry 4IAF[12]). We have not *a priori* discarded or ruled out any of the two mechanisms—associative and dissociative—proposed for PKA.

In order to properly follow the discussion of our results, it is important to distinguish between the γ-oxygen atoms of ATP. Here, the nomenclature of the 4IAC[12] PDB entry was followed (see Figure 2). Thus, both in our initial model as in the starting 4IAC crystallographic structure, O1γATP interacts with crystallographic waters, and it is positioned in front of the Gly-rich loop but around 5 Å away from it; O2γATP coordinates the Mg2 ion and forms a 2.8 Å hydrogen bond with the ε-ammonium group of Lys168; and, finally, O3γATP coordinates the Mg1 ion.

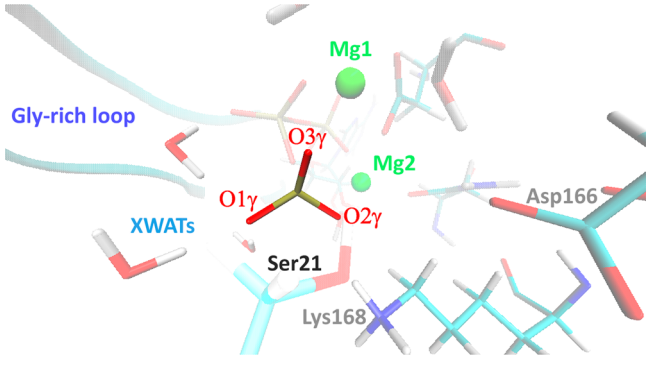

Figure 2. Schematic representation of the γ-oxygen atoms of ATP and the chemical environment that distinguishes each one.

Comparison between the Initial Theoretical Model and the X-Ray Crystallographic Model. It is worth comparing first the 4IAC X-ray structure of the PKAc-AMP-PCPMg_2−SP20 complex with the QM/MM optimized initial model (i_{model} in Tables 1−4) of the solvated PKAc-ATPMg_2−SP20 complex. One geometric feature, specially noted by Gerlits et al.,[12] of the starting 4IAC crystallographic structure was the relative orientation of the OH group of the substrate $Ser21_{SP20}$, which directly affected the assembly of hydrogen bonds within the chemically active region. Thus, as referred by the authors[12] and summarized in Tables 1−4, in 4IAC, the hydroxyl group of the substrate serine is at 3.5 Å from the γ-phosphorus atom of ATP, it lacks the hydrogen bond to Asp166, and it is rotated toward O3γATP (the γ-oxygen atom also coordinated to Mg1) forming a hydrogen bond with a OγSer21-O3γATP distance of 2.7 Å. The authors also reported a $Ser21_{SP20}$ Oγ-Cβ-Cα-N torsion angle of 64°. As expected, the active site of our computationally obtained initial structure is geometrically comparable to that of the crystallographic structure. The OγSer21-O3γATP distance (2.7 Å), which corresponds to a HγSer21-O3γATP distance of 1.81 Å, and the long OγSer21-Oδ2Asp166 distance (4.3 Å) are maintained, with an almost identical $Ser21_{SP20}$ Oγ-Cβ-Cα-N torsion angle (69°). From a geometric point of view, both structures (4IAC and i_{model}) could be considered to be prone to the associative phosphoryl transfer path, with the O3γATP as direct proton acceptor in the incoming phosphate group.

On the other hand, it is also important to highlight that the presence of ATP in the i_{model} structure did not modify the Gly-rich loop position found in the starting 4IAC crystallographic structure, with this loop in both of them somewhat displaced relative to its position in most of the other crystallographic[14,20,69−71] and theoretical[24−26,28,30,32,33] structures characterized for the different stages of the phosphoryl transfer reaction. Such displacement is considered by Gerlits et al.[12] to be due to the strong steric effects of the β,γ-methylene group in AMP-PCP, acting as ATP-analogue, in such a way that the Gly-rich loop is pushed farther from the phosphorylated tail of the ATP kinase cofactor. In contrast, the fact of restituting the β,γ-bridging oxygen of ATP results in the recovery of the octahedral coordination of the Mg2 ion (Mg2−O3βATP distance of 3.3 Å in 4IAC and 3.0 Å in i_{model}), whereas the Mg2 ion coordination in 4IAC is trigonal bipyramidal due to the incapacity of the β,γ-bridging CH_2 group in AMP-PCP to bind to a metal ion.[12] Moreover, because of the shorter distance of the β,γ-bridging bond in ATP than in AMP-PCP, the γ-phosphate group in the i_{model} structure retracts into the ADP moiety (PγATP-OγSer21 distance of 3.5 Å in 4IAC and 3.8 Å in i_{model}, respectively (see Tables S1−S4 in the Supporting Information (SI)).

Reaction Paths and Stationary Points Computationally Determined. From the i_{model} structure, it was possible to simulate both the associative and dissociative mechanisms. In fact, as detailed below, our calculations show the viability of two of the three analyzed associative reaction pathways, each one involving a particular γ-oxygen atom of ATP as the proton acceptor, specifically, O1γATP and O3γATP. For both associative paths, three forward/backward cycles of associative R4-reaction coordinate scans were sufficient to reach a converged potential energy profile. It has to be underlined that this concatenation of successive forward/backward cycles

DOI: 10.1021/acscatal.5b01064
ACS Catal. 2015, 5, 4897−4912

Table 1. Selected QM(B3LYP/6-31+G(d))/CHARMM Bond Distances (Å), Bond Angles (deg), and Dihedrals (deg) in the Optimized Reactants (Ra3), Transition State (TSa3), and Products (Pa3) for the Associative Mechanism with the O3γATP as the Proton Acceptor (O3γATP-Associative Path); Comparison with Values from X-ray Crystallographic Structures Characterizing the Different Stages of the Phosphoryl Transfer Mechanism Catalyzed by the PKA[a]

	4IAC[12]	i_{model}	Ra3	TSa3	Pa3	1L3R[14]	4IAF[12]
O3βATP-PγATP	1.8*	1.70	1.70	1.78	2.89	2.3*	4.1
PγATP-OγSer21	3.5	3.76	3.27	2.26	1.64	2.3*	1.6
OγSer21-HγSer21	---	0.98	0.98	1.64	2.50	---	---
O3γATP-HγSer21	---	1.81	2.04	1.01	0.99	---	---
OγSer21-Oδ2Asp166	4.4	4.28	3.40	3.63	3.54	2.5	4.7
$angle_{O3\beta ATP\text{-}P\gamma ATP\text{-}O\gamma Ser21}$	148.2*	141.3	166.5	164.6	171.2	162.6*	159.8
$angle_{O\gamma Ser21\text{-}H\gamma Ser21\text{-}O3\gamma ATP}$	---	153.6	145.2	127.5	80.3	---	---
$d._{Ser21(N-C\alpha-C\beta-O\gamma)}$	64.0	68.7	−69.9	−59.2	−48.7	−64.8	74.0
$d._{Asp166(C\beta-C\gamma-O\delta2)-O2\gamma ATP}$	160.0	167.2	159.0	154.1	148.6	117.8*	−119.2*
							−152.5*
							−104.8*

[a]Nomenclature is based on the PDB entry of 4IAC[12] X-ray crystallographic structure. For 4IAC[12] * is O3βATP = CβAMP-PCP; for 1L3R[14] * γPO3 = AlF3; for 4IAF[12] * means that is not possible to establish the chemical correspondence of the OiγATP atoms in relation to the 4IAC[12] PDB entry nomenclature.

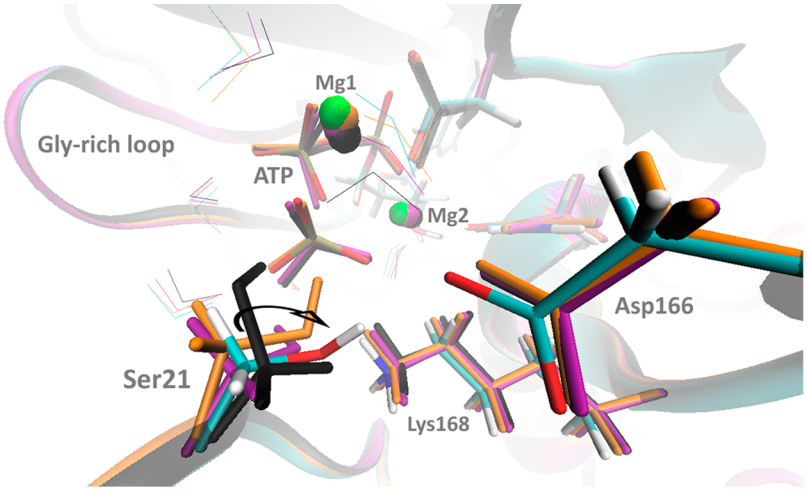

Figure 3. Superposition of the active sites of the optimized initial model (i_{model}, colored in black), O3γATP-associative reactive complex (Ra3, colored in orange), O1γATP-associative reactive complex (Ra1, colored in purple), and dissociative reactive complex (Rd, colored by atom type).

along the reaction coordinate up to the convergence is achieved considerably relaxes the system and contributes to eliminate artificial strains. It is worth mentioning that when simulating the O2γATP-associative path, the HγSer21 atom was transferred to Oδ2Asp166, so following a dissociative path, instead of being transferred directly to the recipient ATP's γ-oxygen atom. On the other hand, for the dissociative mechanism, also two of the three possible pathways for the second step of the mechanism were found to be plausible, each one involving as the final proton acceptor a particular γ-oxygen atom of the phosphoryl group already bonded to the substrate $Ser21_{SP20}$, specifically, O2γATP and O3γATP. For the common phosphoryl transfer step, four forward/backward cycles of dissociative R4-reaction coordinate scans were needed to obtain a converged potential energy profile. Further, for the second step of the dissociative mechanism, that is, the proton transfer from the protonated Asp166 to the just phosphorylated substrate, four and three forward/backward cycles of dissociative R2-reaction coordinate scans were needed to reach a converged potential energy profile with O2γATP and O3γATP as proton acceptor, respectively. As described below, when analyzing the results for the dissociative phosphoryl transfer, the O1γATP-path for this proton transfer step is sterically hindered.

As a result of scanning until convergence, the reaction coordinates required to model the aforementioned mechanistic alternatives of the catalyzed phosphoryl transfer reaction, specific Michaelis complexes were characterized in each case, with significant geometric differences in the active site between them and the i_{model} (Tables 1−4). In the geometry of all the Michaelis complexes localized in the simulated phosphoryl transfer QM/MM reaction paths, the substrate serine's hydroxyl group is rotated toward the carboxylate group of Asp166, presenting a Oγ-Cβ-Cα-N torsion angle of −70°, −39°, and −57° in the O3γATP-associative (Ra3), O1γATP-associative (Ra1), and dissociative (Rd) reactive complex, respectively (see Figure 3). Moreover, although in such structures the β,γ-bridging bond of ATP does not change from its value in i_{model} (1.7 Å), the PγATP-OγSer21 distance does change: the oxygen atom of the nucleophilic hydroxyl group is closer to the phosphorus atom of the γ-phosphate of ATP in Ra3 (3.3 Å), Ra1 (3.1 Å), and Rd (3.4 Å) structures, than in the 4IAC crystallographic starting structure (3.5 Å) and in i_{model} (3.8 Å). In addition, the PγATP-OγSer21 interaction is

DOI: 10.1021/acscatal.5b01064
ACS Catal. 2015, 5, 4897−4912

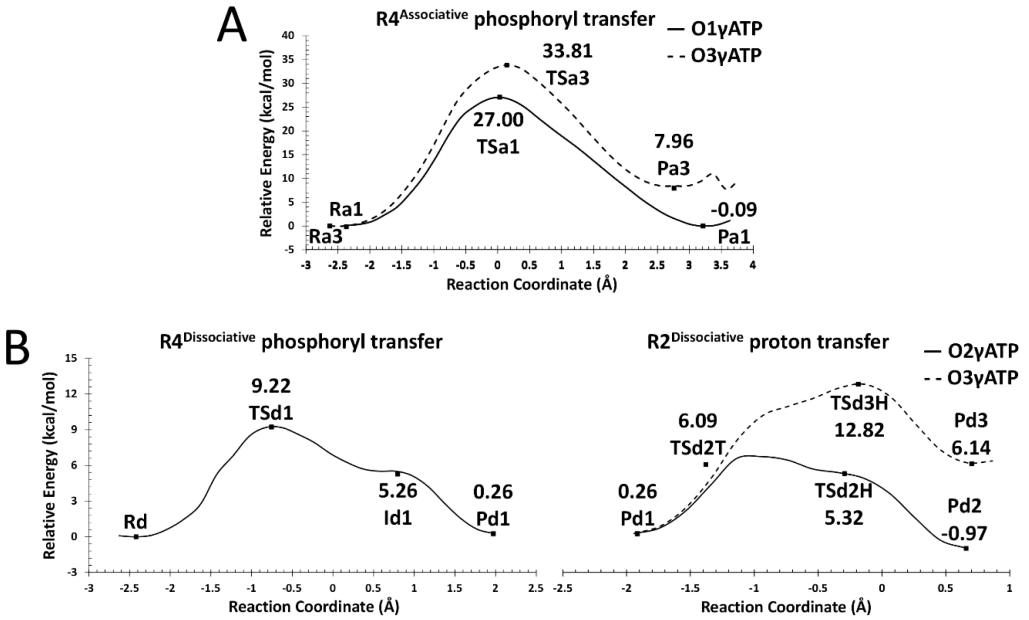

Figure 4. Calculated B3LYP/6-31+G(d)/CHARMM potential energy profiles, potential energy barriers, and reaction potential energies along (A) the R4 reaction coordinate for the associative phosphoryl transfer step, and (B) the R4 and R2 reaction coordinates for the dissociative phosphoryl transfer and proton transfer steps, respectively. The energy barriers and the reaction energies correspond to the stationary points located as described in the Models and Methods section.

Table 2. Selected QM(B3LYP/6-31+G(d))/CHARMM Bond Distances (Å), Bond Angles (deg), and Dihedrals (deg) in the Optimized Reactants (Ra1), Transition State (TSa1), and Products (Pa1) for the Associative Mechanism with the O1γATP as the Proton Acceptor (O1γATP-Associative Path); Comparison with Values from X-ray Crystallographic Structures Characterizing the Different Stages of the Phosphoryl Transfer Mechanism Catalyzed by the PKA[a]

	4IAC[12]	i_{model}	Ra1	TSa1	Pa1	1L3R[14]	4IAF[12]
O3βATP-PγATP	1.8*	1.70	1.70	1.76	2.93	2.3*	4.1
PγATP-OγSer21	3.5	3.76	3.11	2.27	1.64	2.3*	1.6
OγSer21-HγSer21	---	0.98	0.98	1.57	2.91	---	---
O1γATP-HγSer21	---	3.12	1.94	1.03	0.99	---	---
OγSer21-Oδ2Asp166	4.4	4.28	4.01	4.2	3.5	2.5	4.7
$angle_{O3\beta ATP\text{-}P\gamma ATP\text{-}O\gamma Ser21}$	148.2*	141.3	174.2	167.1	171.8	162.6*	159.8
$angle_{O\gamma Ser21\text{-}H\gamma Ser21\text{-}O1\gamma ATP}$	---	153.6	151.8	130.7	59.1	---	---
$d._{Ser21(N-C\alpha\text{-}C\beta\text{-}O\gamma)}$	64.0	68.7	−39.3	−40.9	−46.5	−64.8	74.0
$d._{Asp166(C\beta\text{-}C\gamma\text{-}O\delta2)\text{-}O2\gamma ATP}$	160.0	167.2	158.7	147.9	142.3	117.8*	−119.2*
							−152.5*
							−104.8*

[a]Nomenclature is based on the PDB entry of 4IAC[12] X-ray crystallographic structure. For 4IAC[12] * is O3βATP = CβAMP-PCP; for 1L3R[14] * γPO3 = AlF3; for 4IAF[12] * means that is not possible to establish the chemical correspondence of the OiγATP atoms in relation to the 4IAC[12] PDB entry nomenclature.

almost linearly aligned to the β,γ-bridging bond of the ATP molecule (see $angle_{O3\beta ATP\text{-}P\gamma ATP\text{-}O\gamma Ser21}$ in Tables 1−4, which takes values closer to 180° than those present in the i_{model} and 4IAC structures). Moreover, the hydroxyl group of the $Ser21_{SP20}$ side chain interacts through a 2.9 Å hydrogen bond with O3γATP and O1γATP in Ra3 and Ra1, respectively, whereas in Rd, it interacts with the Oδ2Asp166 through a 2.8 Å hydrogen bond (all those values correspond to O−O distances). Thus, compared to i_{model} and regardless of the phosphoryl transfer reaction channel that each one defines geometrically, it is clear that all three converged reactive complexes have been reached after a conformational change in the $Ser21_{SP20}$ side chain, and with this new configuration, the γ-phosphate group of ATP cofactor is closer to the substrate's nucleophilic γ-oxygen atom. Thus, the computationally obtained ternary complex structures seem to be more directed to the corresponding chemical step than the preceding model structures (4IAC and i_{model}).

The QM/MM potential energy profiles at the (B3LYP/6-31+G(d))/MM level along (A) the associative and (B) the dissociative reaction coordinates are shown in Figure 4. For the associative profiles, the γ-oxygen atom of ATP acting as the proton acceptor is indicated in each case. The dissociative potential energy profile includes the results for the simulation of the second proton transfer, from the Oδ2Asp166 to both the O2γATP and the O3γATP atoms, where the change in the reaction coordinate variable should be noted. The related QM/MM potential energy barriers and reaction energies are depicted in the corresponding reaction profile.

I. Associative Pathway. As can be seen in Figure 4A, the reaction path that was characterized from the O1γATP-associative reactive complex is energetically favored over the

DOI: 10.1021/acscatal.5b01064
ACS Catal. 2015, 5, 4897−4912

Table 3. Selected QM(B3LYP/6-31+G(d))/CHARMM Bond Distances (Å), Bond Angles (deg), and Dihedrals (deg) in the Optimized Reactants (Rd), Phosphoryl-Transfer Transition State (TSd1), Proton Shift Intermediate (Id1), Phosphoryl-Transfer Products (Pd1), Asp166 Side Chain-Rotation Transition State (TSd2T), Proton-Transfer Transition State (TSd2H), and Proton-Transfer Products (Pd2) for the Dissociative Mechanism with the O2γATP as the Final Proton Acceptor (O2γATP-Dissociative Path); Comparison with Values from X-ray Crystallographic Structures Characterizing the Different Stages of the Phosphoryl Transfer Mechanism Catalyzed by the PKA[a]

	4IAC[12]	i_{model}	Rd	TSd1	Id1	Pd1	TSd2T	TSd2H	Pd2	1L3R[14]	4IAF[12]
O3βATP-PγATP	1.8*	1.70	1.76	2.31	2.89	3.02	3.05	3.47	3.39	2.3*	4.1
PγATP-OγSer21	3.5	3.76	3.36	2.36	1.87	1.74	1.69	1.66	1.64	2.3*	1.6
OγSer21-HγSer21	---	0.98	0.99	1.00	1.12	1.67	2.31	2.76	2.57	---	---
Oδ2Asp166-HγSer21	---	4.23	1.81	1.71	1.35	1.02	0.99	1.11	1.67	---	---
O2γATP-HγSer21	---	3.52	3.26	2.82	2.76	2.93	2.37	1.40	1.01	---	---
OγSer21-Oδ2Asp166	4.4	4.28	2.80	2.71	2.46	2.66	3.17	3.49	3.57	2.5	4.7
Oδ2Asp166-O2γATP	3.8	3.93	3.82	3.59	3.47	3.52	3.11	2.49	2.68	3.1*	3.3*
											5.4*
											5.8*
$angle_{O3\beta ATP\text{-}P\gamma ATP\text{-}O\gamma Ser21}$	148.2*	141.3	167.7	168.4	166.2	166.3	170.8	178.3	172.0	162.6*	159.8
$angle_{O\gamma Ser21\text{-}H\gamma Ser21\text{-}O\delta 2Asp166}$	---	86.4	173.3	172.0	169.3	162.2	145.3	123.0	113.1	---	---
$angle_{O\delta 2Asp166\text{-}H\gamma Ser21\text{-}O2\gamma ATP}$	---	60.2	93.6	101.6	110.8	117.8	130.8	164.4	172.5	---	---
$d._{Ser21(N-C\alpha\text{-}C\beta\text{-}O\gamma)}$	64.0	68.7	−56.8	−48.1	−42.9	−43.2	−60.7	−73.5	−70.1	−64.8	74.0
$d._{Asp166(C\beta\text{-}C\gamma\text{-}O\delta 2)\text{-}O2\gamma ATP}$	160.0	167.2	119.6	118.4	118.7	124.5	145.8	172.4	175.0	117.8*	−119.2*
											−152.5*
											−104.8*

[a]Nomenclature is based on the PDB entry of 4IAC[12] X-ray crystallographic structure. For 4IAC[12] * is O3βATP = CβAMP-PCP; for 1L3R[14] * γPO3 = AlF3; for 4IAF[12] * means that is not possible to establish the chemical correspondence of the OiγATP atoms in relation to the 4IAC[12] PDB entry nomenclature.

one defined from the O3γATP-associative reactive complex (27.0 and 33.8 kcal/mol potential energy barriers, respectively). This was not the expected result because the geometry of the preceding i_{model} and 4IAC crystallographic structures pointed out to a reactive path in which the hydroxyl group of serine's side chain could directly protonate O3γATP before the phosphoryl transfer. Moreover, both associative reaction paths involve higher potential energy barriers for the phosphoryl transfer than that calculated for the dissociative counterpart (9.2 kcal/mol, Figure 4B). The calculated reaction potential energies describe two almost isoergic processes for both the O1γATP-associative and the dissociative phosphoryl transfer paths (−0.1 and 0.3 kcal/mol, respectively), whereas that for the O3γATP-associative is endoergic (8.0 kcal/mol). A general point to be noted is that along all the obtained reaction paths, the significant structural changes within the reactive core occur with almost no rearrangement in the rest of the ternary complex model.

The Ra3 and Ra1 associative reactants complexes evolve to their corresponding products complexes, through the TSa3 and TSa1 transition states, respectively. The geometric parameters presented in Tables 1 and 2 show that the nucleophilic attack in both reaction channels takes place with an O3βATP-PγATP-OγSer21 bond angle of 165° and 167° at TSa3 and TSa1, respectively, and when ADP and the γ-phosphate leaving group are still bonded (O3βATP-PγATP bond distance of 1.8 Å at TSa3 and TSa1). To reach those structures, the proton transfer—from the nucleophilic hydroxyl group of $Ser21_{SP20}$ to the corresponding γ-oxygen atom of ATP's terminal phosphate group—anticipates the phosphoryl transfer. Consequently, the distance from the OγSer21 atom to the proton-acceptor γ-oxygen atom decreases to 2.3 Å along the reaction coordinate's segment describing the initial proton transfer process. This, in turn, facilitates the breaking of the β,γ-bridging bond of ATP along the nucleophilic displacement. However, although this preliminary H-shift process increases the nucleophilicity of OγSer21, it also involves important geometric constraints (particularly for the HγSer21-OγSer21-PγATP-OiγATP ring[25]), so that an extra energy penalty must be overcome by the reacting atoms to reach a configuration prone for the nucleophilic attack, that is, with a short enough PγATP-OγSer21 distance, and an almost linear O3βATP-PγATP-OγSer21 bond angle, as in both TSa3 and TSa1 structures. In our previous work about the plausibility of the PKA's associative reaction pathway with the heptapeptide Kemptide as substrate,[32] a potential energy barrier of 21.3 kcal/mol was reported for the reaction channel with the chemically equivalent O1γATP atom as the proton acceptor (named there as O3γATP according to 1CDK crystallographic structure). The lower potential energy barrier in that case is a consequence of a less restrained transition state compared to the TSa1 structure. On the other hand, in both TSa3 and TSa1, the calculated transition vectors (with associated imaginary frequencies of 228i and 141i cm^{-1}, respectively) clearly characterize the nucleophilic substitution, although with some contribution from the movement of the shifted-proton. The PγATP-OγSer21 bond is clearly formed in Pa3 and Pa1 (1.64 Å), and a 2.9 Å O3βATP-PγATP distance in both of them is in clear agreement with previous theoretical results for PKA-catalyzed phosphorylation product complexes, for which the phosphoryl transfer process has been considered effectively completed.[25,26,28,32]

As mentioned before, within the associative mechanism and for our PKAc ternary complex model, the computed energy barriers given in Figure 4A clearly favor the reaction channel with the O1γATP atom as the proton acceptor over that obtained with O3γATP. This trend is in agreement with our previous results with Kemptide as substrate and PKAc described by the 1CDK crystallographic structure.[32] In summary, the transfer of HγSer21 to O1γATP causes the

DOI: 10.1021/acscatal.5b01064
ACS Catal. 2015, 5, 4897−4912

Table 4. Selected QM(B3LYP/6-31+G(d))/CHARMM Bond Distances (Å), Bond Angles (deg), and Dihedrals (deg) in the Optimized Reactants (Rd), Phosphoryl-Transfer Transition State (TSd1), Proton Shift Intermediate (Id1), Phosphoryl-Transfer Products (Pd1), Proton-Transfer Transition State (TSd3H), and Proton-Transfer Products (Pd3) for the Dissociative Mechanism with the O3γATP as the Final Proton Acceptor (O3γATP-Dissociative Path); Comparison with Values from X-ray Crystallographic Structures Characterizing the Different Stages of the Phosphoryl Transfer Mechanism Catalyzed by the PKA[a]

	4IAC[12]	i_{model}	Rd	TSd1	Id1	Pd1	TSd3H	Pd3	1L3R[14]	4IAF[12]
O3βATP-PγATP	1.8*	1.70	1.76	2.31	2.89	3.02	3.21	3.15	2.3*	4.1
PγATP-OγSer21	3.5	3.76	3.36	2.36	1.87	1.74	1.66	1.64	2.3*	1.6
OγSer21-HγSer21	---	0.98	0.99	1.00	1.12	1.67	2.69	2.56	---	---
Oδ2Asp166-HγSer21	---	4.23	1.81	1.71	1.35	1.02	1.14	1.71	---	---
O3γATP-HγSer21	---	1.81	3.20	2.92	2.83	2.95	1.33	1.00	---	---
OγSer21-Oδ2Asp166	4.4	4.28	2.80	2.71	2.46	2.66	3.56	3.46	2.5	4.7
Oδ2Asp166-O3γATP	4.3	4.49	3.81	3.61	3.39	3.33	2.43	2.71	3.4*	3.3*
										5.4*
										5.8*
$angle_{O3\beta ATP\text{-}P\gamma ATP\text{-}O\gamma Ser21}$	148.2*	141.3	167.7	168.4	166.2	166.3	161.9	167.4	162.6*	159.8
$angle_{O\gamma Ser21\text{-}H\gamma Ser21\text{-}O\delta 2Asp166}$	---	86.4	173.3	172.0	169.3	162.2	131.7	106.5	---	---
$angle_{O\delta 2Asp166\text{-}H\gamma Ser21\text{-}O3\gamma ATP}$	---	86.2	94.4	99.0	102.4	102.9	159.0	175.0	---	---
$d_{\cdot Ser21(N-C\alpha\text{-}C\beta\text{-}O\gamma)}$	64.0	68.7	−56.8	−48.1	−42.9	−43.2	−45.7	−45.3	−64.8	74.0
$d_{\cdot Asp166(C\beta\text{-}C\gamma\text{-}O\delta 2)\text{-}O3\gamma ATP}$	−105.5	−96.1	49.4	69.4	85.5	110.2	−176.6	−171.6	−88.4*	−119.2*
										−152.5*
										−104.8*

[a]Nomenclature is based on the PDB entry of 4IAC[12] X-ray crystallographic structure. For 4IAC[12] * is O3βATP = CβAMP-PCP; for 1L3R[14] * γPO3 = AlF3; for 4IAF[12] * means that is not possible to establish the chemical correspondence of the OiγATP atoms in relation to the 4IAC[12] PDB entry nomenclature.

remaining γ-phosphoryl negative charge to accumulate in the O2γATP and O3γATP atoms, where it is more readily stabilized by means of the already existing coordination interactions with the Mg^{2+} ions (see Table S2 in the SI). On the contrary, the transfer of HγSer21 to O3γATP disturbs the coordination sphere of the Mg1 ion to which that γ-oxygen atom is bonded (see Table S1 in the SI).

Regarding the O3γATP- and O1γATP-associative product complexes (the Pa3 and Pa1 structures, respectively), it can be observed that the coordination of both Mg^{2+} ions is octahedral, and it is almost identical to that in the corresponding reactant complex structures (Ra3 and Ra1, respectively), with the exception of the Mg2−O3βATP interaction. Specifically, such interaction is strengthened due to the stabilization by the Mg2 metal ion of the negative charge that accumulates on the β,γ-bridging oxygen as the β,γ-phosphoanhydride bond of ATP is broken due the nucleophilic attack of OγSer17 on PγATP (see Mg^{2+} ions coordination sphere in Table S1 and Table S2 in the SI). Moreover, as it is also observed in all the optimized stationary points along the O3γATP- and O1γATP-associative paths, the NζLys168 forms strong hydrogen bonds with OγSer21 and O2γATP (see the catalytic core interaction distances in Table S1 and Table S2 in the SI). We will go deep into this observation when comparing the final products complexes of the dissociative mechanism with the 4IAF structure, because those interactions are also found there.

II. Dissociative Pathway. The calculated potential energy barriers and reaction potential energies for the complete dissociative mechanism appear summarized in Figure 4B. For the phosphoryl transfer step (see $R4^{Dissociative}$ phosphoryl transfer profile), besides the corresponding transition state (TSd1) and products complex (Pd1), we were able to characterize an intermediate structure (Id1) connecting both of them (see structures in Figures S1−S3, in the SI). The inspection of the TSd1 structure (Table 3 or Table 4) reveals that the nucleophilic attack takes place when the γ-phosphoryl group—in a planar configuration—is in a quasi-symmetrical position between the leaving O3βATP (2.31 Å) and the entering OγSer21 (2.36 Å) oxygen atoms. That is, within a trigonal bipyramidal coordination around the reacting γ-phosphorus atom, in the TSd1 structure, the O3βATP-PγATP bond is almost completely broken when the PγATP-OγSer21 bond-forming interaction begins to strengthen. These results are in excellent agreement with that for the TS mimic 1L3R X-ray structure,[14] in which the γ-phosphoryl group is replaced by the planar AlF_3 group, showing distances of 2.3 Å to the ADP moiety and substrate serine (see structural data given in Table 3 and Figure 5). The same concordance can be established for the O3βATP-PγATP-OγSer21 angle (consistent with a nearly in-line mechanism) and for the orientation of Asp166 side chain relative to the γ-phosphoryl group (Asp166(Cβ-Cγ-Oδ2)-O2γATP dihedral). The most significant difference between both structures is related with the conformation of the Gly-rich loop shown in Figure 5b. However, it is relevant to highlight that both loop conformations with Ser53-Gly186 distances of 11.01 Å for TSd1 and 10.38 Å for 1L3R, respectively, clearly belong to the so-called closed conformational state defined by Ser53-Gly186 distances within the range 11 ± 2 Å.[6] In fact, recent MD simulations have also shown[6] that the ternary complex PKA-ATP-substrate displays higher root-mean-square fluctuation (RMSF) values for all the relevant catalytic loops and, in particular, for the Gly-rich loop in comparison with the dynamics of the PKA-ATP-inhibitor complex. The flexibility of the Gly-rich loop is then a dynamic feature of the reactive closed conformations of the PKA-ATP-substrate. It seems that this motion is not catalytically relevant if the closed conformation is maintained. Frequency calculations confirmed a single imaginary frequency mode of 75i cm^{-1}, with the transition vector accounting for the nucleophilic attack exclusively and, thus, without any contribution related with

DOI: 10.1021/acscatal.5b01064
ACS Catal. 2015, 5, 4897−4912

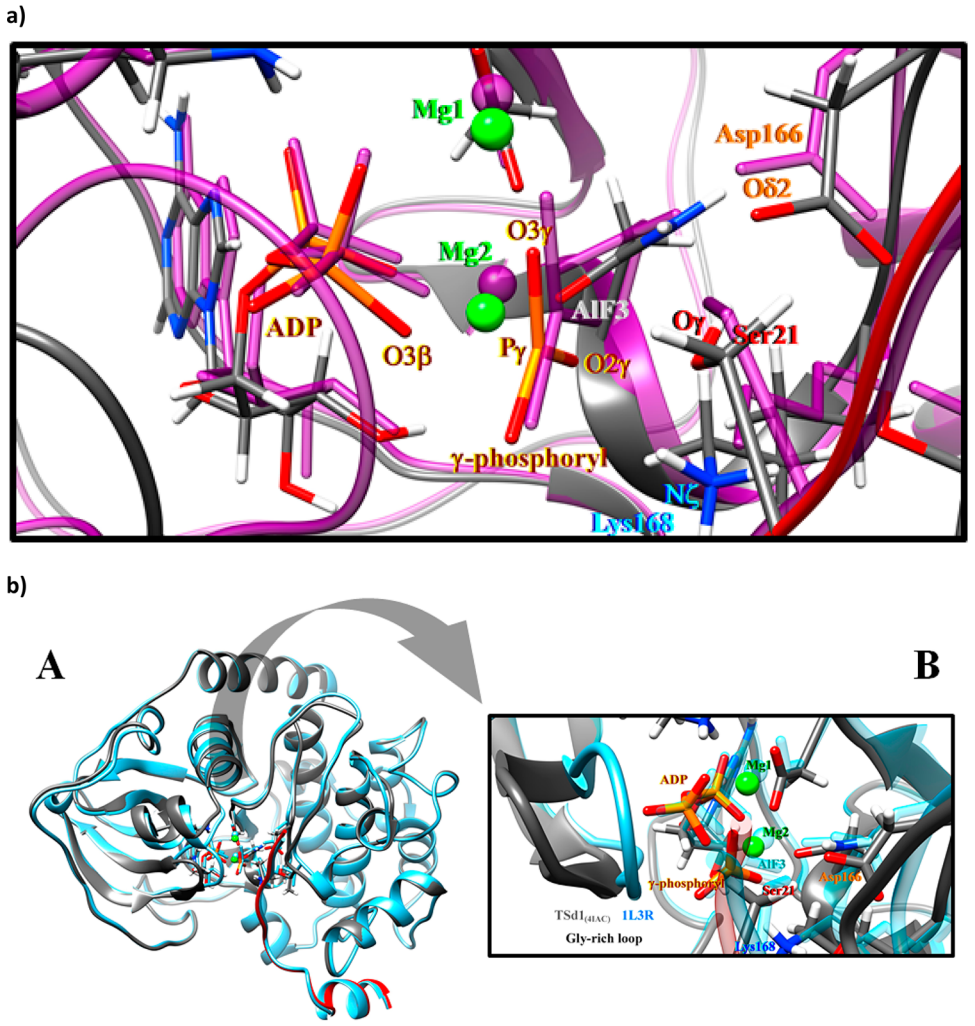

Figure 5. (a) Overlay between the catalytic cores of the phosphoryl-transfer transition state structure of the dissociative mechanism (TSd1) (in sticks colored by element) and the transition state mimic crystallographic structure (1L3R) (in purple sticks); (b) A: Global overlay of the TSd1 (gray) and 1L3R (blue) structures; B: In the inset, an enlarged view of the active site showing the different conformation of the Gly-rich loop in both structures (sticks colored by element correspond to the Tsd1 structure and sticks in blue correspond to the 1L3R structure).

the movement of the serine hydroxyl hydrogen toward the carboxylate side chain of Asp166.

Thus, along the phosphoryl transfer step of the dissociative mechanism, HγSer21 is not promptly shifted from the substrate hydroxyl to the nascent phosphoryl group. Rather, it is delivered to the carboxylate group of the highly conserved Asp166 residue after the phosphoryl transfer. Then, in going from the TSd1 to the Pd1 phosphoryl-transfer products complex (i.e., the phosphorylated substrate, pSP20), the reaction path describes a plateau (0.5 Å < R4 < 1.0 Å values) involving a set of geometries that were used as starting points for searching a transition state structure that could characterize such proton transfer to the Asp166 side chain. However, such structure was not found. The related Id1 intermediate structure lays 4.0 kcal/mol below TSd1 and 5.0 kcal/mol above Pd1. Although this Id1 formally fulfills the conditions for a shallow minimum, it should be rather considered as a shoulder along the reaction path. Essentially, while the γ-phosphoryl group continues moving away from ADP (O3βATP-PγATP 2.89 Å) and its bond with the substrate serine is significantly formed (PγATP-OγSer21 1.87 Å), when arriving at the Id1 structure, the OγSer21 atom interacts through a very short hydrogen bond with the Oδ2Asp166 atom (2.46 Å), so that the related proton transfer event takes place without any additional energy cost. Further, in the Pd1 structure the OH bond of the substrate serine is completely broken (1.67 Å), but the hydrogen bond interaction between the now protonated Oδ2Asp166 and the phosphorylated OγSer21 (2.66 Å) is still present, though it is not as short as in Id1 (see Table 3 or 4).

Regarding the octahedral coordination for both Mg^{2+} ions, it remains practically unchanged throughout the phosphoryl transfer step, except for the Lewis acid attack of Mg2 that stabilizes the nascent and leaving ADP moiety. Thus, the initially weakly bound Mg2 metal ion strengthens its interaction with O3βATP by screening the negative charge which accumulates on the β,γ-bridging oxygen concomitant with the cleavage of the O3βATP-PγATP bond. Specifically, the Mg2−O3βATP distance decreases almost to its final value as the molecular complex evolves through the transition state region (TSd1).

In Pd1, the O2γATP and O3γATP atoms of the phosphorylated $Ser21_{SP20}$ are both reachable (from a sterically point of view) from the just protonated Oδ2Asp166, whereas the O1γATP is much farther away, and the proton transfer to such oxygen atom would have to occur through—or in the immediate vicinity of—the newly formed PγATP-OγSer21

DOI: 10.1021/acscatal.5b01064
ACS Catal. 2015, 5, 4897−4912

bond, thus distorting it severely. Therefore, only the proton transfer paths corresponding to the protonation of the phosphorylated SP20 substrate at O2γATP and O3γATP were explored (see Figure 4B, $R2^{Dissociative}$ proton transfer profiles).

Specifically, the O2γATP-path goes through a transition state structure (TSd2T) that represents a potential energy barrier of 6.1 kcal/mol (i.e., 5.8 kcal/mol over Pd1 and approximately 3 kcal/mol lower than the barrier corresponding to the phosphoryl transfer step). The TSd2T structure is characterized by a transition vector (44i cm^{-1}) that corresponds to the rotation of the protonated side chain of Asp166 toward the O2γATP atom. This movement, from Pd1 to TSd2T, can also be assessed from the increase of the Asp166(Cβ-Cγ-Oδ2)-O2γATP dihedral and the decrease in the Oδ2Asp166-O2γATP distance (see Table 3; accordingly, the OγSer21-Oδ2Asp166 distance increases). After passing TSd2T, these trends continue, and the molecular complex evolves through another transition state structure, the TSd2H (localized around a R2 value of −0.25 Å), whose transition vector (179i cm^{-1}) characterizes the proton transfer from the protonated Asp166 to O2γATP. Specifically, Oδ2Asp166 and O2γATP interact strongly through a short hydrogen bond (2.49 Å). Furthermore, a Oδ2Asp166-HγSer21-O2γATP angle of 164° and a Asp166(Cβ-Cγ-Oδ2)-O2γATP dihedral of 172° also account for the clear orientation of the Asp166 side chain's protonated carboxylic oxygen toward the proton-acceptor O2γATP atom of the phosphorylated $Ser21_{SP20}$. Energetically, TSd2H represents a 5.3 kcal/mol potential energy barrier with respect to the reactant complex structure. That is, 5 kcal/mol over Pd1 and 0.8 kcal/mol more stable than the preceding TSd2T structure. We were not able to computationally define a stable intermediate connecting both transition state structures. This can be explained in terms of the quite planar region of the O2γATP-potential energy profile that goes from TSd2T to TSd2H. Finally, after going through TSd2H, the HγSer21 proton is completely transferred to O2γATP (1.01 Å), forming the Pd2 final product structure, in which the Oδ2Asp166 and O2γATP atoms are still tightly hydrogen-bonded (at a distance of 2.68 Å, and with an Oδ2Asp166-HγSer21-O2γATP angle of 173°). Moreover, the final PγATP-OγSer21 distance at P2 of 1.64 Å is in good agreement with that in the 4IAF X-ray structure of the PKAc−Mg_2ADP−pSP20 ternary complex. The global reaction potential energy is −1.0 kcal/mol with respect to the reactant complex, so that the overall PKA dissociative phosphoryl transfer mechanism is slightly exoergic when following the O2γATP-path for the second proton transfer.

On the other hand, regarding the O3γATP-path for the proton transfer step, although the protonated side chain of Asp166 also rotates toward O3γATP when evolving from Pd1, the rotation takes place now along the uphill region of the corresponding potential energy profile (around a R2 value of −1.0 Å, see Figure 4B), in such a way that it does not constitute an independent chemical step by itself. Thus, the O3γATP-path reaches the TSd3H transition state structure that characterizes the proton transfer with a transition vector (710i cm^{-1}) with a unique contribution from the movement of the transferred proton. Energetically, TSd3H is 12.8 kcal/mol less stable than the reactive complex Rd (a potential energy barrier almost 7 kcal/mol higher than TSd2T and TSd2H). As it happens in TSd2H, the HγSer21 proton is completely transferred to O3γATP (with a O3γATP-HγSer21distance of 1.00 Å), and the Oδ2Asp166 atoms interacts strongly with O3γATP through a short hydrogen bond (2.43 Å) (see Table 4). The proton transfer to the O3γATP of the phosphorylated substrate results in the formation of the Pd3 products complex structure, which entails a 6.1 kcal/mol reaction potential energy. That is, the O3γATP-path for the proton transfer step gives a final product 7 kcal/mol less stable than the O2γATP-path.

The proton transfer from Oδ2Asp166 to O2γATP clearly destabilizes the Mg2−O2γATP interaction (the Mg2−O2γATP distance increases from 2.15 Å at Pd1 to 3.33 Å at TSd2H, and then remains almost constant, attaining a value of 3.25 Å at Pd2; see Table S3 in the SI). In contrast, the protonation of O3γATP does not entail such a separation from Mg1 (the Mg1−O3γATP distance only increases from 2.03 Å at Pd1 to 2.20 Å at Tsd3H, and then to 2.32 Å at Pd3; see Table S4 in the SI). That is, after the phosphoryl transfer step, the negative charge on O2γATP is less stabilized by Mg2 than the negative charge on O3γATP by Mg1, and then O2γATP has a stronger basic character—with respect to the HγSer21 protonating the Asp166's carboxylate—than O3γATP. This explains why the O2γATP-path for the proton transfer step is favored over the O3γATP-path.

The comparison of the dissociative final product complex structures with the 4IAF crystallographic product complex, reveals significant differences related with the stage of the catalytic cycle represented in each case. In the Pd2 structure, although O2γATP is farther from Mg2 than in the Pd3 structure, it is not far enough to completely lose its interaction to Mg2. On the other hand, NζLys168 is strongly hydrogen-bonded to the O2γATP throughout the dissociative phosphoryl transfer and both proton transfer O2γATP- and O3γATP-paths (see Tables S3 and S4 in the SI). Moreover, along the dissociative phosphoryl transfer, NζLys168 also forms a hydrogen bond with the OγSer21. This interaction remains strong all through the proton transfer O3γATP-path, and is somewhat weaker along the O2γATP-path. In very good agreement, both interactions are also present in the PKAc TS mimic and the PKAc ATP-hydrolysis products crystallographic structures (PDB codes 1L3R[14] and 4DH5,[69] respectively). In contrast, these geometric features significantly differ from what is observed in the PKAc products complex 4IAF crystallographic structure. According to Gerlits et al.,[12] as a consequence of the displacement of the γ-phosphate onto the $Ser21_{SP20}$, in 4IAF, the Mg2 divalent cation no longer interacts with the O2γATP but does so with a new water molecule. This relevant change in the coordination sphere of the Mg2 ion along the catalytic mechanism has been recently observed also in two crystallographic structures of PKA-Mg_2AMP-PNP-SP20 showing partial or total phosphoryl transfer (4HPU and 4HPT structures, respectively).[13] It is worth mentioning though that the changes in the Mg2 coordination sphere along the dissociative reaction pathway might correlate with the structural changes present at the product complex 4IAF crystallographic structure. After the phoshoryl transfer step, the Mg2 metal ion strengthens its interaction with O3βATP, increasing its binding to the ADP moiety of ATP, whereas Mg1 presents a more labile coordination all the way through. These differences in the coordination spheres of the two Mg ions seem plausible, taking into account that it has recently been proposed and confirmed that only Mg2 remains bound in the active site with ADP after product release.[72] Once the last proton transfer step to O2γ takes place, the Mg2−O2γATP distance clearly increases, and this vacant ligand position could be the one occupied by a water molecule in the 4IAF, as well as in the 4HPU and 4HPT

DOI: 10.1021/acscatal.5b01064
ACS Catal. 2015, 5, 4897−4912

structures to maintain the octahedral coordination. The Mg1 coordination sphere does not change so much along the chemical process, so the changes observed in the different experimental product complex structures (mostly due to the growing distance of Asp184) must be more related with the product release process.

Further, in 4IAF the phosphate group now bonded to $Ser21_{SP20}$ does not form any hydrogen bond with Asp166 or with Lys168, but it does form a bond with the side chain's OH group of Ser53, interaction that is neither present in the 4IAC starting structure, nor in the i_{model} nor along the associative and dissociative paths and the corresponding optimized stationary points here reported. Gerlits et al.[12] relate these observations with the fact that the CβSer21-OγSer21 bond is rotated away from the reaction core toward the bulk solvent so that the product can be released from the enzyme. That is, our results suggest that while the product complex structures theoretically calculated and presented in this work correspond to the final stage of the phosphoryl transfer chemical reaction, the 4IAF structure would represent a snapshot of the phosphorylated substrate release progression. That is the reason why, in contrast to what is found in the 4IAF crystallographic structure, we do not find the interaction between Ser53 residue and the phosphate group of Ser21 in either of the theoretically determined products (Pd2 and Pd3 structures). These structures are the final products of the complete phosphoryl transfer from ATP to the substrate, and in both of them, the phosphate group of Ser21 is still interacting, via hydrogen bond, with the carboxylate group of Asp166. From this point, the substrate is ready to evolve to its release from the active site. The dynamic character of a protein system allows the rotation of the Ser21 Cα-Cβ bond of the substrate that might eventually break the hydrogen bond between the phosphate group of Ser21 and Asp166 residue and lead the phosphate to interact with Ser53 in the Gly-rich loop. The visual inspection of the Pd2 and Pd3 product structures indicates that this rotation is possible in their active site, and it would had probably occurred if we had studied the product release step by molecular dynamics simulation. However, this is beyond the scope of our paper, which is focused on the simulation of the complete phosphoryl transfer from ATP to the SP20 substrate catalyzed by the PKA enzyme.

To complete the energetic analysis we have performed single-point energy evaluations at the MP2/aug-cc-pVTZ/CHARMM level of theory on the B3LYP/6-31+G(d)/CHARMM stationary points (see Table 5). The results confirm the preference of the dissociative mechanism over the associative mechanism for the phosphoryl transfer catalyzed by PKA, with quite comparable potential energy barrier results at the DFT and MP2 levels. However, for the second step of the dissociative mechanism, the high-level potential energy barrier at TSd2H that characterizes the proton transfer to O2γATP as the final proton acceptor, is just 2 kcal/mol lower than that for the proton transfer to O3γATP at TSd3H (6.8 and 8.8 kcal/mol, respectively), while at the DFT level, such difference is 7.5 kcal/mol (5.3 and 12.8 kcal/mol, respectively). Furthermore, the overall reaction potential energy at the MP2 level is also very similar (1.5 and 3.2 kcal/mol for the O2γATP- and O3γATP-dissociative path, respectively), whereas this is not the case at the DFT level (−1.0 and 6.1 kcal/mol, respectively). The difference in the proton transfer barriers when comparing the MP2 and DFT results could be attributed either to the fact that MP2 barriers derive from single-point energy calculations or to an overpolarization of the QM electron density by the MM point charges when using the B3LYP functional and diffuse functions that tend to delocalize the extra electron corresponding to the total charge of the QM region (−1).

Table 5. Potential Energy Barriers and Reaction Potential Energies (in kcal/mol) Corresponding to the MP2/aug-cc-pVTZ/CHARMM Single-Point Calculations on the B3LYP/6-31+G(d)/CHARMM Stationary Points

O3γATP-associative		O1γATP-associative		dissociative	
phosphoryl transfer		*phosphoryl transfer*		*phosphoryl transfer*	
Ra3	---	Ra1	---	Rd	---
TSa3	31.30	TSa1	23.26	TSd1	9.52
Pa3	6.42	Pa1	−3.88	Id1	2.26
				Pd1	−2.68
				proton transfer to O2γATP	
				TSd2T	2.17
				TSd2H	6.84
				Pd2	1.47
				proton transfer to O3γATP	
				TSd3H	8.80
				Pd3	3.19

4. DISCUSSION

In this manuscript, the two proposed mechanisms (dissociative and associative) for the phosphorylation reaction of the SP20 substrate catalyzed by PKA have been analyzed by means of MP2/aug-cc-pVTZ/CHARMM//B3LYP/6-31+G(d)/CHARMM calculations using a complete solvated model of the PKAc-ATPMg_2−SP20 system. Flexible reaction coordinates have been used in order to properly explore the potential energy surface for this reaction. Using the 4IAC X-ray structure of the PKAc-AMP-PCPMg_2−SP20 complex as initial template for our *in silico* calculations, four reaction pathways for the phosphorylation reaction were found connecting reactants and products. In agreement with our previous results[32,33] for the phosphorylation of the heptapeptide substrate known as Kemptide, the associative mechanism consists of a one-step reaction with a transition state corresponding to the γ-phosphoryl transfer from ATP to the nucleophilic hydroxyl group of $Ser21_{SP20}$. The nucleophilicity of $Ser21_{SP20}$ is enhanced by an early proton transfer from this substrate's OH group to one of the Oγ-ATP atoms. Of the three possible associative pathways, only the two corresponding to O1γATP and O3γATP, acting as proton acceptors, have been located on the potential energy surface. The O1γATP-pathway is favored over the O3γATP one because the negative charge excess on the phosphate group is better stabilized over O2γATP and O3γATP which belong to the coordination spheres of Mg2 and Mg1, respectively. On the other hand, the dissociative mechanism consists of two steps associated with two different molecular processes. The first step is the phosphoryl transfer that imposes the first potential energy barrier. In this mechanism, the nucleophilicity of $Ser21_{SP20}$ is enhanced, in part, by the hydrogen-bond between the hydroxyl group of $Ser21_{SP20}$ and the carboxylate group of the highly conserved Asp166 residue. Following the phosphoryl transfer, a proton migration from the hydroxyl group of $Ser21_{SP20}$ to Asp166 takes place without potential energy barrier even though an intermediate structure for this proton transfer has been located

DOI: 10.1021/acscatal.5b01064
ACS Catal. 2015, 5, 4897−4912

that presents a very short hydrogen-bond. In the second step, Asp166 delivers back the proton to the phosphorylated product. In this way, Asp166 behaves as a base catalyst favoring the phosphoryl transfer and as an acid catalyst protonating the phosphorylated substrate and regenerating the original protonation state of the enzyme. Of the three possible proton transfer pathways, only the two corresponding to O2γATP and O3γATP as proton acceptors have been located. Their respective potential energy barriers are quite similar. Anyway it has to be mentioned that Asp166 acts neither as a conventional acid catalyst nor a conventional base catalyst in the dissociative mechanism, because both proton transfers happen quite late along the corresponding reaction paths. The late proton-transfer when Asp166 behaves as a base catalyst is consistent with previous results.[14,24−26,28] However, the proton transfer from $Ser21_{SP20}$ to Asp166 and then the protonation of the phosphorylated product by Asp166 are required for the enzyme reaction to proceed through a dissociative mechanism.

In agreement with our previous calculations with Kemptide,[32,33] the dissociative mechanism results are clearly favored with respect to the associative process. For both substrates, the dissociative mechanism presents the same two steps, that is, phosphoryl transfer and protonation of the phosphorylated substrate. In fact, the potential energy barriers for each one of these two mechanistic steps are quite similar for both substrates: 9.5 and 10.9 kcal/mol for the phosphoryl transfer with SP20 and Kemptide, respectively, and 6.8 (or 8.8) and 7.8 kcal/mol for the protonation of SP20 and Kemptide, respectively. So this study, based on the molecular simulation of the phosphorylation reaction, demonstrates that the PKAc catalytic mechanism is not substrate-dependent as previously suggested. However, the product complexes, with the unprotonated (for the first step) and the protonated phosphorylated peptide (for the second step) of the mechanism, are clearly better stabilized in the active site in the case of SP20. This would be in agreement with the tighter binding of pSP20 in comparison with phosphokemptide that dissociates very fast.[20] In fact, Taylor and coworkers have attributed their own recent success of trapping stable PKAc−ADP Mg2−pSP20 product complexes in crystals to the unique binding properties of this substrate peptide.[12,13] In addition, the greater stabilization of the unprotonated phosphorylated SP20 peptide in our calculations allows us to predict that the global chemical process for the SP20 phosphorylation is faster than for Kemptide.

On the other hand, the comparison between the phosphoryl-transfer transition state structures for SP20 and Kemptide reveals significant differences. With both reaction paths dissociative, at the two transition states, the nucleophile and leaving groups are bonded to the γ-phosphorus to rather differing extent. The phosphoryl-transfer transition state for SP20 presents very similar O3βATP-PγATP bond-breaking and PγATP-OγSer21 bond-forming distances, whereas at the corresponding transition state for Kemptide, the O3βATP-PγATP distance is much longer than the PγATP-OγSer21 one. At both transition states, though, the γ-PO3 group has a planar configuration with the phosphorus atom bearing a similar trigonal bipyramidal coordination. The degree of coupling between the phosphoryl-transfer process and the proton transfer from $Ser21_{SP20}$ to Asp166 is different in the two transition states. So, the transition vector of the SP20 transition state accounts for the nucleophilic attack exclusively, whereas there is a clear contribution related with the movement of the serine hydroxyl hydrogen toward the carboxylate side chain of Asp166 in the transition vector of the corresponding transition state for Kemptide.

The comparison of the stationary points structures for the SP20 phosphorylation by PKA, located along the QM/MM reaction pathway, with the crystallographic structures for the PKAc-AMPPCPMg_2−SP20 complex (4IAC), for the transition state mimic (1L3R), and for the PKAc-ADPMg_2-pSP20 complex (4IAF), reveals very interesting details of the different molecular stages of the PKA catalytic cycle. First, we confirm that 4IAC can be a good structure to be taken as starting point to progress not only via the associative pathway, as suggested by Gerlits et al.,[12] but also along the dissociative mechanism. The substrate serine's Oγ-Cβ-Cα-N torsion angle (defined by Gerlits et al. as the "reaction driving force")[12] is confirmed here as an important geometrical parameter to characterize the structural advance of the catalytic process. The $Ser21_{SP20}$ hydroxyl group is directed outward the catalytic core (toward the solvent) at 4IAC, but it rotates toward the carboxylate group of Asp166 when the chemical reaction initiates and remains in this orientation all along the chemical steps of the associative and dissociative pathways. The same orientation of the $Ser21_{SP20}$ hydroxyl group is found in the 1L3R crystallographic structure corresponding to a transition state mimic of the phosphorylation reaction. The excellent agreement between the 1L3R structure and the geometry of the dissociative transition state stationary point located on the dissociative pathway validates our *in silico* model, on one hand, and supports the preference for the dissociative mechanism, although representative conformations of the Michaelis complex could follow both mechanisms. In the 4IAF structure, the phosphoryl group transferred to $Ser21_{SP20}$ is directed again outward the catalytic core (toward the solvent), indicating that the 4IAF structure could represent a more advanced stage of the catalytic cycle when the phosphorylated substrate release takes place, whereas the product complex structures located on the calculated reaction pathways correspond to the final stage of the chemical process. We are aware that a complete study of the reaction mechanism of this highly flexible enzyme would require an extensive treatment of the dynamics of the system. The calculation of only reaction paths is not enough for the enzyme to visit all thermally accessible nuclear configurations of the system and to describe the effect of all possible reorientations of the different residues. However, we have described here a reaction path that can help to understand the main trends of the reaction, and that turns out to be quite plausible when compared with the available crystal structures.

Our calculations show for the first time the viability of the SP20 phosphorylation process in a conformation of the PKAc-ATPMg_2−SP20 ternary complex in which the Gly-rich loop is somewhat displaced with respect to the fully closed conformation of the PKAc-ATPMg_2−IP20 complex. Many recent experimental and theoretical results have revealed the high degree of flexibility of the Gly-rich loop, so the possibility that this loop might adopt different conformations in the reactive ternary complexes is not discarded. Along the associative and dissociative paths here simulated, the Gly-rich loop maintains its initial conformation at the 4IAC structure, so it is not really a flap at the mouth of the active site's cleft like in more closed conformations, even though it cannot be described as an open configuration either. Further, even though the apparently preferred Gly-rich loop position for the catalytic reaction is not restituted, the phosphorylated tail of ATP can

DOI: 10.1021/acscatal.5b01064
ACS Catal. 2015, 5, 4897−4912

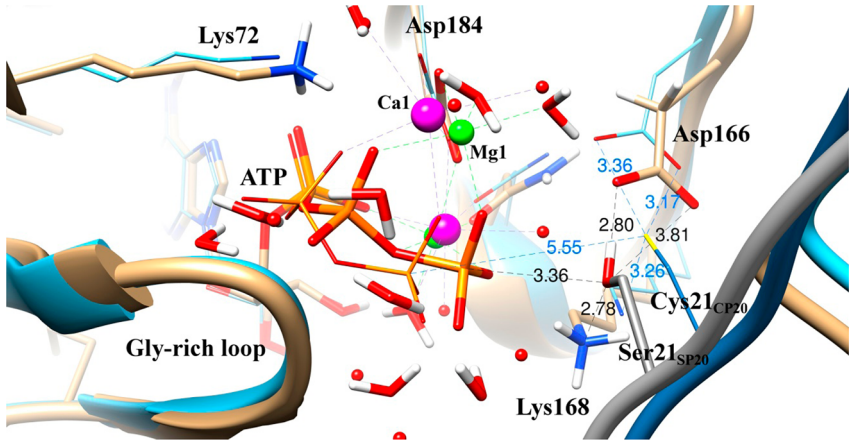

Figure 6. Global overlay of the Rd (khaki, with SP20 in gray) and 4XW5 (cyan, with CP20 in steel blue) structures. The catalytic cores of Rd and 4XW5 are represented in thick- and thin-sticks, respectively, both colored by atom type. In Rd, Mg^{2+} ions are green, while in 4XW5, Ca^{2+} ions are magenta.

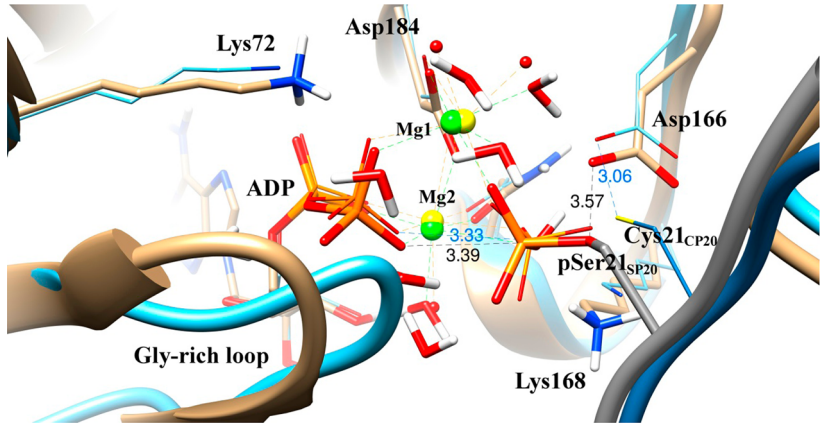

Figure 7. Global overlay of the Pd2 (khaki, with SP20 in gray) and 4XW6 (cyan, with CP20 in steel blue) structures. The catalytic cores of Pd2 and 4XW6 are represented in thick- and thin-sticks, respectively, both colored by atom type. In Pd2, Mg^{2+} ions are green, while in 4XW6, Mg^{2+} ions are yellow.

still be stabilized through strong hydrogen bonds with three crystallographic waters all along the characterized stationary points of the PKA-catalyzed phosphoryl transfer. The presence of those water molecules substitutes the stabilizing interactions between the Gly-rich loop residues and ATP, previously observed in the closed conformation. In particular, our results confirm, in agreement with mutagenesis experiments,[9] that the OH side-chain of Ser53 is not needed for the catalytic reaction taking place in the active site of PKAc. In fact, in this conformation of the Gly-rich loop none of the interactions between the backbone-nitrogen atoms of residues 53−55 with the Oγ atoms of ATP is present.

After submission of this paper, new crystallographic structures were determined[73] by three of the authors that published the 4IAC structure. As indicated by these authors, the search of new crystallographic structures is motivated by the objective of finding a better model of the ternary PKA-ATP-SP20 Michaelis complex. Previous crystallographic structures mimicking the reactant complex were obtained either with peptide inhibitors or ATP analogues, as is the case of the 4IAC structure. The recent crystallization of the ternary complex PKAc-Ca_2ATP-CP20, where, with respect to 4IAC, the substrate $Ser21_{SP20}$ has been substituted by Cys21, Mg^{2+} by Ca^{2+}, and AMP-PCP by ATP, results in a structure (PDB code 4XW5) where the main artifact caused by the presence of an ATP analogue in 4IAC is overcome. That is, the $Cys21_{CP20}$ is now facing Asp166, ready to undergo the phosphoryl transfer step assisted by the base catalyst Asp166. At this point, we believe that it is worthy to mention that our optimized reactant structure (labeled as Rd in this paper) is validated by the 4XW5 structure, because the orientation of the catalytic residues in both structures is highly comparable (see Figure 6). Remarkably, the substrate $Ser21_{SP20}$ is orientated toward the catalytic residue Asp166 in the optimized structure (interaction distance of 2.8 Å) analogously to $Cys21_{CP20}$ toward Asp166 in the 4XW5 structure (interaction distance of 3.2 Å). Thus, in spite of the initial position of Ser21, rotated by ≈110° away from Asp166 in both the 4IAC structure and the initial theoretical i_{model}, the optimization process has driven Ser21 to a position where it forms a hydrogen bond with Asp166, which is a necessary step to initiate the phosphoryl transfer via the dissociative mechanism. Figure 6 allows us to compare another two interaction distances found in both the Rd reactant and the 4XW5 structure. In both cases, Lys168 forms a hydrogen bond with the side chain of the residue 21 of the substrate, and the measured distances are comparable: 2.8 Å for the Lys168-O_γ-Ser21 distance in Rd in comparison to a distance Lys168-S_γ-Cys21 of 3.4 Å in 4XW5. The different sizes of sulfur and

DOI: 10.1021/acscatal.5b01064
ACS Catal. 2015, 5, 4897−4912

oxygen atoms may explain the difference. In contrast, the comparison of the distance between the Pγ atom of ATP and the substrate nucleophile atom (O_γ or S_γ in SP20 or CP20, respectively) seems to indicate that the 4XW5 crystallographic structure represents a previous stage, in comparison to the Rd structure, of the catalytic cycle process. That is, the reactive fragments are still far away (5.6 Å) from each other in 4XW5, whereas they are at a near attack (3.4 Å interaction distance) conformation in R_d. Finally, it is clear from inspection of Figure 6 that the Gly-rich loop position (see the bottom-left side of the Figure) is comparable in both structures.

On the other hand, Figure 7 compares the recent crystallographic structure of the ternary complex PKAc-Mg_2ADP-PO_4−CP20 (PDB file 4XW6), which mimics a product state immediately after the phosphoryl transfer has taken place,[73] with our Pd2 product structure. As mentioned above in relation to the Rd and 4XW5 structures, the new 4XW6 structure validates our model of phosphoryl transfer product. In both Pd2 and 4XW6, the catalytic Asp166 residue is facing the phosphoryl group, in agreement with its proposed role as the acid catalyst that protonates the phosphoryl group of the product. The comparison of the distances, shown in Figure 7, between Asp166 and the O_γ and S_γ atoms in Pd2 and 4XW6 structures, respectively, together with the broken P_γ-O_β bond distances in both structures, give us a quantitative indication of the correspondence between the crystallographic and the computationally determined structures. Thus, and in contrast to the 4IAF structure, our results indicate that the recently determined 4XW6 structure and our optimized model of the phosphoryl transfer product represent the same stage of the catalytic cycle.

In summary, at the end of the work described here, we have for the first time an accurate comparison of X-ray and theoretically determined structures that represent the evolution of the enzymatic system along the catalytic process. Specifically, our results complete the data experimentally determined about the nature of the transition state and highlight important features of the chemical step and its relation with the enzyme dynamics.

■ ASSOCIATED CONTENT

Supporting Information

The Supporting Information is available free of charge on the ACS Publications website at DOI: 10.1021/acscatal.5b01064.

Selected QM(B3LYP/6-31+G(d))/CHARMM bond distances, bond angles, and dihedrals in the optimized reactants, intermediates, transition states, and products for the associative and dissociative mechanisms. Molecular views of the active site at the different stationary points of the associative and dissociative mechanisms (PDF)

■ AUTHOR INFORMATION

Corresponding Author

*E-mail: Angels.Gonzalez@uab.cat.

Notes

The authors declare no competing financial interest.

■ ACKNOWLEDGMENTS

We thank the Spanish Ministerio de Economía y Competitividad (Grant CTQ2011-24292 and Grant CTQ2014-53144-P) for financial support. A.P.-G. acknowledges "Consejo Nacional de Ciencia y Tecnología" (CONACYT) Supporting Grant 213582. We also acknowledge CSUC for computational facilities.

■ REFERENCES

(1) Cohen, P. *Eur. J. Biochem.* **2001**, *268*, 5001−5010.
(2) Knighton, D.; Zheng, J.; Ten Eyck, L.; Ashford, V.; Xuong, N.; Taylor, S.; Sowadski, J. *Science* **1991**, *253*, 407−414.
(3) Knighton, D.; Zheng, J.; Ten Eyck, L.; Xuong, N.; Taylor, S.; Sowadski, J. *Science* **1991**, *253*, 414−420.
(4) Johnson, D. A.; Akamine, P.; Radzio-Andzelm, E.; Madhusudan; Taylor, S. S. *Chem. Rev.* **2001**, *101*, 2243−2270.
(5) Adams, J. A. *Chem. Rev.* **2001**, *101*, 2271−2290.
(6) Masterson, L. R.; Cembran, A.; Shi, L.; Veglia, G. *Adv. Protein Chem. Struct. Biol.* **2012**, *87*, 363−389.
(7) Taylor, S. S.; Zhang, P.; Steichen, J. M.; Keshwani, M. M.; Kornev, A. P. *Biochim. Biophys. Acta, Proteins Proteomics* **2013**, *1834*, 1271−1278.
(8) Bjarnadottir, U.; Nielsen, J. E. *Biopolymers* **2012**, *97*, 65−72.
(9) Aimes, R. T.; Hemmer, W.; Taylor, S. S. *Biochemistry* **2000**, *39*, 8325−8332.
(10) Masterson, L. R.; Cheng, C.; Yu, T.; Tonelli, M.; Kornev, A.; Taylor, S. S.; Veglia, G. *Nat. Chem. Biol.* **2010**, *6*, 821−828.
(11) Masterson, L. R.; Shi, L.; Metcalfe, E.; Gao, J.; Taylor, S. S.; Veglia, G. *Proc. Natl. Acad. Sci. U. S. A.* **2011**, *108*, 6969−6974.
(12) Gerlits, O.; Waltman, M. J.; Taylor, S.; Langan, P.; Kovalevsky, A. *Biochemistry* **2013**, *52*, 3721−3727.
(13) Bastidas, A. C.; Deal, M. S.; Steichen, J. M.; Guo, Y.; Wu, J.; Taylor, S. S. *J. Am. Chem. Soc.* **2013**, *135*, 4788−4798.
(14) Madhusudan; Akamine, P.; Xuong, N.-H.; Taylor, S. S. *Nat. Struct. Biol.* **2002**, *9*, 273−277.
(15) Bao, Z. Q.; Jacobsen, D. M.; Young, M. A. *Structure* **2011**, *19*, 675−690.
(16) Jacobsen, D. M.; Bao, Z.-Q.; O'Brien, P.; Brooks, C. L.; Young, M. A. *J. Am. Chem. Soc.* **2012**, *134*, 15357−15370.
(17) Gerlits, O.; Das, A.; Keshwani, M. M.; Taylor, S.; Waltman, M. J.; Langan, P.; Heller, W. T.; Kovalevsky, A. *Biochemistry* **2014**, *53*, 3179−3186.
(18) Montenegro, M.; Masgrau, L.; González-Lafont, À.; Lluch, J. M.; Garcia-Viloca, M. *Biophys. Chem.* **2012**, *161*, 17−28.
(19) Zhang, P.; Smith-Nguyen, E. V.; Keshwani, M. M.; Deal, M. S.; Kornev, A. P.; Taylor, S. S. *Science* **2012**, *335*, 712−716.
(20) Madhusudan; Trafny, E. A.; Xuong, N.-H.; Adams, J. A.; Eyck, L. F. T.; Taylor, S. S.; Sowadski, J. M. *Protein Sci.* **1994**, *3*, 176−187.
(21) Gibbs, C. S.; Zoller, M. J. *J. Biol. Chem.* **1991**, *266*, 8923−8931.
(22) Zhou, J.; Adams, J. A. *Biochemistry* **1997**, *36*, 15733−15738.
(23) Lew, J.; Taylor, S. S.; Adams, J. A. *Biochemistry* **1997**, *36*, 6717−6724.
(24) Valiev, M.; Kawai, R.; Adams, J. A.; Weare, J. H. *J. Am. Chem. Soc.* **2003**, *125*, 9926−9927.
(25) Díaz, N.; Field, M. J. *J. Am. Chem. Soc.* **2004**, *126*, 529−542.
(26) Cheng, Y.; Zhang, Y.; McCammon, J. A. *J. Am. Chem. Soc.* **2005**, *127*, 1553−1562.
(27) Cheng, Y.; Zhang, Y.; McCammon, J. A. *Protein Sci.* **2006**, *15*, 672−683.
(28) Valiev, M.; Yang, J.; Adams, J. A.; Taylor, S. S.; Weare, J. H. *J. Phys. Chem. B* **2007**, *111*, 13455−13464.
(29) Montenegro, M.; Garcia-Viloca, M.; González-Lafont, À.; Lluch, J. *J. Comput.-Aided Mol. Des.* **2007**, *21*, 603−615.
(30) Montenegro, M.; Garcia-Viloca, M.; Lluch, J. M.; Gonzalez-Lafont, A. *Phys. Chem. Chem. Phys.* **2011**, *13*, 530−539.
(31) Smith, G. K.; Ke, Z.; Guo, H.; Hengge, A. C. *J. Phys. Chem. B* **2011**, *115*, 13713−13722.
(32) Pérez-Gallegos, A.; Garcia-Viloca, M.; González-Lafont, À.; Lluch, J. *J. Comput.-Aided Mol. Des.* **2014**, *28*, 1077−1091.
(33) Pérez-Gallegos, A.; Garcia-Viloca, M.; González-Lafont, À.; Lluch, J. M. *Phys. Chem. Chem. Phys.* **2015**, *17*, 3497−351.

DOI: 10.1021/acscatal.5b01064
ACS Catal. 2015, 5, 4897−4912

(34) Prasad, B. R.; Plotnikov, N. V.; Warshel, A. *J. Phys. Chem. B* **2013**, *117*, 153−163.
(35) Plotnikov, N. V.; Prasad, B. R.; Chakrabarty, S.; Chu, Z. T.; Warshel, A. *J. Phys. Chem. B* **2013**, *117*, 12807−12819.
(36) Brünger, A. T.; Karplus, M. *Proteins: Struct., Funct., Genet.* **1988**, *4*, 148−156.
(37) Brooks, B. R.; Bruccoleri, R. E.; Olafson, B. D.; States, D. J.; Swaminathan, S.; Karplus, M. *J. Comput. Chem.* **1983**, *4*, 187−217.
(38) Brooks, B. R.; Brooks, C. L.; Mackerell, A. D.; Nilsson, L.; Petrella, R. J.; Roux, B.; Won, Y.; Archontis, G.; Bartels, C.; Boresch, S.; Caflisch, A.; Caves, L.; Cui, Q.; Dinner, A. R.; Feig, M.; Fischer, S.; Gao, J.; Hodoscek, M.; Im, W.; Kuczera, K.; Lazaridis, T.; Ma, J.; Ovchinnikov, V.; Paci, E.; Pastor, R. W.; Post, C. B.; Pu, J. Z.; Schaefer, M.; Tidor, B.; Venable, R. M.; Woodcock, H. L.; Wu, X.; Yang, W.; York, D. M.; Karplus, M. *J. Comput. Chem.* **2009**, *30*, 1545−1614.
(39) MacKerell, A. D.; Bashford, D.; Bellott, M.; Dunbrack, R. L.; Evanseck, J. D.; Field, M. J.; Fischer, S.; Gao, J.; Guo, H.; Ha, S.; Joseph-McCarthy, D.; Kuchnir, L.; Kuczera, K.; Lau, F. T. K.; Mattos, C.; Michnick, S.; Ngo, T.; Nguyen, D. T.; Prodhom, B.; Reiher, W. E.; Roux, B.; Schlenkrich, M.; Smith, J. C.; Stote, R.; Straub, J.; Watanabe, M.; Wiórkiewicz-Kuczera, J.; Yin, D.; Karplus, M. *J. Phys. Chem. B* **1998**, *102*, 3586−3616.
(40) MacKerell, A. D.; Feig, M.; Brooks, C. L. *J. Am. Chem. Soc.* **2003**, *126*, 698−699.
(41) Sherwood, P.; de Vries, A. H.; Guest, M. F.; Schreckenbach, G.; Catlow, C. R. A.; French, S. A.; Sokol, A. A.; Bromley, S. T.; Thiel, W.; Turner, A. J.; Billeter, S.; Terstegen, F.; Thiel, S.; Kendrick, J.; Rogers, S. C.; Casci, J.; Watson, M.; King, F.; Karlsen, E.; Sjøvoll, M.; Fahmi, A.; Schäfer, A.; Lennartz, C. *J. Mol. Struct.: THEOCHEM* **2003**, *632*, 1−28.
(42) Ahlrichs, R.; Bär, M.; Häser, M.; Horn, H.; Kölmel, C. *Chem. Phys. Lett.* **1989**, *162*, 165−169.
(43) Slater, J. C. *Phys. Rev.* **1951**, *81*, 385−390.
(44) Vosko, S. H.; Wilk, L.; Nusair, M. *Can. J. Phys.* **1980**, *58*, 1200−1211.
(45) Becke, A. D. *Phys. Rev. A: At., Mol., Opt. Phys.* **1988**, *38*, 3098−3100.
(46) Becke, A. D. *J. Chem. Phys.* **1993**, *98*, 5648−5652.
(47) Stephens, P. J.; Devlin, F. J.; Chabalowski, C. F.; Frisch, M. J. *J. Phys. Chem.* **1994**, *98*, 11623−11627.
(48) Lee, C.; Yang, W.; Parr, R. G. *Phys. Rev. B: Condens. Matter Mater. Phys.* **1988**, *37*, 785−789.
(49) Hehre, W. J.; Ditchfield, R.; Pople, J. A. *J. Chem. Phys.* **1972**, *56*, 2257−2261.
(50) Hariharan, P. C.; Pople, J. A. *Theoret. Chim. Acta* **1973**, *28*, 213−222.
(51) Francl, M. M.; Pietro, W. J.; Hehre, W. J.; Binkley, J. S.; Gordon, M. S.; DeFrees, D. J.; Pople, J. A. *J. Chem. Phys.* **1982**, *77*, 3654−3665.
(52) Clark, T.; Chandrasekhar, J.; Spitznagel, G. W.; Schleyer, P. V. R. *J. Comput. Chem.* **1983**, *4*, 294−301.
(53) Smith, W.; Forester, T. R. *J. Mol. Graphics* **1996**, *14*, 136−141.
(54) Montenegro, M.; Garcia-Viloca, M.; González-Lafont, À.; Lluch, J. *Theor. Chem. Acc.* **2009**, *124*, 197−215.
(55) Senn, H. M.; Thiel, W. *Angew. Chem., Int. Ed.* **2009**, *48*, 1198−1229.
(56) de Vries, A. H.; Sherwood, P.; Collins, S. J.; Rigby, A. M.; Rigutto, M.; Kramer, G. J. *J. Phys. Chem. B* **1999**, *103*, 6133−6141.
(57) Sherwood, P.; de Vries, A. H.; Collins, S. J.; Greatbanks, S. P.; Burton, N. A.; Vincent, M. A.; Hillier, I. H. *Faraday Discuss.* **1997**, *106*, 79−92.
(58) Nocedal, J. *Math. Comp.* **1980**, *35*, 773−782.
(59) Liu, D.; Nocedal, J. *Math. Prog.* **1989**, *45*, 503−528.
(60) Turner, A. J.; Moliner, V.; Williams, I. H. *Phys. Chem. Chem. Phys.* **1999**, *1*, 1323−1331.
(61) Billeter, S. R.; Turner, A. J.; Thiel, W. *Phys. Chem. Chem. Phys.* **2000**, *2*, 2177−2186.
(62) Banerjee, A.; Adams, N.; Simons, J.; Shepard, R. *J. Phys. Chem.* **1985**, *89*, 52−57.
(63) Baker, J. *J. Comput. Chem.* **1986**, *7*, 385−395.
(64) Pople, J. A.; Binkley, J. S.; Seeger, R. *Int. J. Quantum Chem.* **1976**, *10*, 1−19.
(65) Head-Gordon, M.; Pople, J. A.; Frisch, M. J. *Chem. Phys. Lett.* **1988**, *153*, 503−506.
(66) Dunning, T. H. *J. Chem. Phys.* **1989**, *90*, 1007−1023.
(67) Woon, D. E.; Dunning, T. H. *J. Chem. Phys.* **1993**, *98*, 1358−1371.
(68) Humphrey, W.; Dalke, A.; Schulten, K. *J. Mol. Graphics* **1996**, *14*, 33−38.
(69) Kovalevsky, A. Y.; Johnson, H.; Hanson, B. L.; Waltman, M. J.; Fisher, S. Z.; Taylor, S.; Langan, P. *Acta Crystallogr., Sect. D: Biol. Crystallogr.* **2012**, *68*, 854−860.
(70) Zheng, J.; Trafny, E. A.; Knighton, D. R.; Xuong, N.; Taylor, S. S.; Ten Eyck, L. F.; Sowadski, J. M. *Acta Crystallogr., Sect. D: Biol. Crystallogr.* **1993**, *49*, 362−365.
(71) Bossemeyer, D.; Engh, R. A.; Kinzel, V.; Ponstingl, H.; Huber, R. *EMBO J.* **1993**, *12*, 849−859.
(72) Bastidas, A. C.; Wu, J.; Taylor, S. S. *Biochemistry* **2015**, *54*, 2−10.
(73) Gerlits, O.; Tian, J.; Das, A.; Langan, P.; Heller, T. H.; Kovalevsky, A. *J. Biol. Chem.* **2015**, *290*, 15538−15548.

NOTE ADDED AFTER ASAP PUBLICATION

This paper was published on the Web on July 24, 2015, with two occurrences of 4IAF cited incorrectly as 4IAC. The corrected version was reposted on July 27, 2015.

DOI: 10.1021/acscatal.5b01064
ACS Catal. 2015, 5, 4897−4912